
HIERARCHIC FLOWS TO ESTIMATE AND SAMPLE HIGH-DIMENSIONAL PROBABILITIES

A PREPRINT

Etienne Lempereur^{*1} and Stéphane Mallat^{2,3}

¹Département d'informatique, Ecole normale supérieure, Paris, France

²Collège de France, Paris, France

³Flatiron Institute, New York, USA

May 7, 2024

ABSTRACT

Finding low-dimensional interpretable models of complex physical fields such as turbulence remains an open question, 80 years after the pioneer work of Kolmogorov. Estimating high-dimensional probability distributions from data samples suffers from an optimization and an approximation curse of dimensionality. It may be avoided by following a hierarchic probability flow from coarse to fine scales. This inverse renormalization group is defined by conditional probabilities across scales, renormalized in a wavelet basis. For a φ^4 scalar potential, sampling these hierarchic models avoids the critical slowing down at the phase transition. An outstanding issue is to also approximate non-Gaussian fields having long-range interactions in space and across scales. We introduce low-dimensional models with robust multiscale approximations of high order polynomial energies. They are calculated with a second wavelet transform, which defines interactions over two hierarchies of scales. We estimate and sample these wavelet scattering models to generate 2D vorticity fields of turbulence, and images of dark matter densities.

1 Introduction

Estimating models of high-dimensional probability distributions from data is at the heart of data science and statistical physics. For a physical system at equilibrium, the probability distribution of a field $\varphi \in \mathbb{R}^d$ (such as an image) has a density $p(\varphi) = \mathcal{Z}^{-1} e^{-U(\varphi)}$, where $U(\varphi)$ is the Gibbs energy [LL13]. Learning means approximating and optimizing an estimation of the high-dimensional energy function U , from m data samples $\{\varphi^{(i)}\}_i$ resulting from measurements or numerical simulations. New data can then be generated by sampling the estimated model of p , which is also used to estimate solutions of inverse problems [KS06, ABT18]. The estimation of a Gibbs energy is particularly difficult when φ has long range dependencies, and its dimension d is large. An outstanding problem is to build probabilistic models of turbulent flows, which dates back to the work of Kolmogorov in 1942 [kol41, Kol42].

In statistics, p is estimated by defining an approximation class p_θ and by optimizing θ . These approximation and optimization problems are plagued by the curse of dimensionality. Section 2 reviews both aspects. It includes linear approximations of Gibbs energies, maximum likelihood estimation versus score matching, and sampling by Langevin diffusions. One can define low-dimensional approximation classes if interactions are local within φ , as in Markov random fields [GG84]. The optimization curse is also avoided if the log-Sobolev constant of p remains bounded when d increases [Gro75, Led00, BGL⁺14]. Sadly enough, none of these two properties are satisfied by complex data such as turbulence fields. Addressing the approximation and optimization curse of dimensionality requires introducing more flexible models.

From a cybernetics perspective, Herbert Simons observed that the architecture of most complex systems is hierarchic, in physics, biology, economic, symbolic languages, or social organizations. He argues that it probably results from their dynamic evolution, where intermediate states must be stable [Sim62]. This attractive idea could explain why the curse

*etienne.lempereur@ens.fr

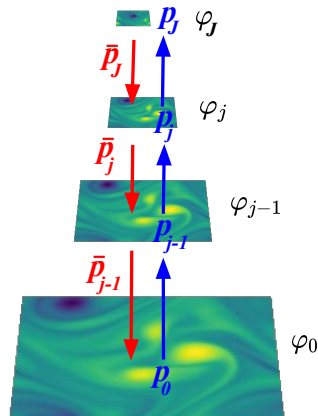


Figure 1: The renormalization group (illustrated in blue) computes the probability distributions $p_j(\varphi_j)$ of images φ_j at progressively larger scales 2^j , with marginal integrations of high-frequency degrees of freedom, up to a maximum scale 2^J . A hierarchic flow (illustrated in red) is a top-down inverse Markov chain which recovers p from p_J by estimating each transition probability \bar{p}_j from p_j to p_{j-1} . Difficulties arise when \bar{p}_j is non-local, as in turbulent flows.

of dimensionality can be avoided when analyzing such systems, but the notion of hierarchy is loosely defined. The core principle of hierarchic organizations is to build long range interactions from a limited number of local interactions between neighbors in the hierarchy. But large systems include multiple hierarchies producing complex long-range interactions in multidimensional matrix organizations, as opposed to a tree. For example, large corporations often include horizontal hierarchic organizations dedicated to specific projects, at each vertical hierarchic level [Tur18]. It creates long-range interactions between employees working on a same project. In physics, the renormalization group theory provides a hierarchic analysis of multiple body interactions. It computes a flow of probabilities from a fine microscopic scale towards larger macroscopic scales [Kad66, Wil71, WF72, Del12].

However, major difficulties have been encountered to take into account non-local interactions in space and across scales. Particularly for non-renormalizable systems such as turbulence, whose degrees of freedom increase with the dimension d of φ [BJPV98].

This paper defines hierarchic models to estimate and sample high-dimensional non-Gaussian processes having non-local interactions. Section 3 considers data $\varphi \in \mathbb{R}^d$ defined on graphs, or images. A first hierarchic organization is constructed with coarse graining approximations φ_j of φ , of progressively smaller sizes as the scale 2^j increases. Figure 1 gives an illustration of the vorticity field of a 2D turbulence. The probability density $p(\varphi)$ is progressively mapped into densities $p_j(\varphi_j)$ from fine to coarse scales 2^j . This renormalization group transformation is computed by marginal integrations of the high frequency degrees of freedom, which progressively disappear as j increases. There is no difficulty to estimate and sample $p_J(\varphi_J)$ if φ_J has a low dimension. From this estimation, the high-dimensional model of p can be estimated and sampled with a reverse Markov chain. It transforms p_J into p by iteratively computing p_{j-1} from p_j , as shown by Figure 1. Each transition kernel \bar{p}_j of this hierarchic flow is the conditional probability of φ_{j-1} given φ_j . The main difficulty is to understand on what conditions one can estimate and sample these transition kernels, without suffering from the curse of dimensionality.

A hierarchic probability flow across scales is an inverse to Wilson renormalization group. If we represent high frequencies in wavelet bases then the transition kernels can be written as conditional probabilities of wavelet coefficients. Renormalizing wavelet coefficients is a strategy to control log-Sobolev constants of transition probabilities. For the φ^4 model of ferromagnetism at phase transition, it was shown in [MOBM22] that a renormalization in a wavelet basis eliminates the "critical slowing down" of Langevin sampling algorithms [ZJ21]. This is verified and analyzed for different types of wavelet bases in Section 4. The φ^4 scalar potential model has local spatial interactions. It is "renormalizable," which means that it can be approximated with a number of coupling parameters, which does not depend on the field dimension d , at all scales. This property does not apply to complex systems such as fluid turbulence, which have progressively more degrees of freedom as the dimension d increases [BJPV98]. To face this issue, we introduce hierarchic potential models, whose dimensions increase when the scale 2^j decreases. The hierarchy preserves a coupling flow equation, which relates the coupling parameters of energies from one scale to the next.

In physics and statistics, Gibbs energies of non-Gaussian probability distributions are often approximated with polynomials of degrees larger than 2, typically 3 or 4 [LL13]. For a stationary field of dimension d , it involves d^2 or d^3 approximation terms, whose estimations have a large variance. Section 5 introduces interaction energy models of dimension $O(\log^3 d)$, with robust multiscale approximations of high order polynomial energies. They are computed with a second wavelet transform, applied to the modulus of the first wavelet transform. It defines a second hierarchy, with a second scale parameter. The resulting scattering coefficients [Mal12] capture long-range non-Gaussian interactions across space and scales [CMA⁺23]. These interaction energy models provide a renormalization group representation of non-renormalizable systems, with $O(\log^3 d)$ degrees of freedom, which increases slowly with the dimension d . Numerical applications are shown to estimate and sample Gibbs energy models of two-dimensional turbulent vorticity fields and dark matter density fields.

2 Probability Models, Estimation and Sampling

We denote by $\varphi \in \mathbb{R}^d$ a data vector of dimension d . We suppose that it has a probability density $p(\varphi) = \mathcal{Z}^{-1} e^{-U(\varphi)}$ with respect to the Lebesgue measure, with a Gibbs energy U which is twice differentiable. Our goal is to estimate an accurate model of p from m samples $\{\varphi^{(i)}\}_{i \leq m}$, and to generate new data by sampling this model. This section is a brief introduction to sampling of high-dimensional probabilities with Langevin diffusions, and to the estimation of parametric models by maximum likelihood and score matching.

2.1 Langevin Sampling and Log Sobolev Inequalities

If $U(\varphi)$ is known, one can sample p with a Langevin dynamics, which is a Markov process that iteratively updates a field φ_t with the stochastic differential equation

$$d\varphi_t = -\nabla_{\varphi} U(\varphi_t) dt + \sqrt{2} dB_t,$$

where B_t is a Brownian motion. It is a gradient descent on the energy, which is perturbed by the addition of a Gaussian white noise. Let φ_0 be a sample of a density p_0 at time $t = 0$. At time t , φ_t is a sample of a density p_t which is guaranteed to converge to the density p of Gibbs energy $U(\varphi)$ [LS16]. The unique invariant measure of this Markov chain is p . We can thus sample p by running Langevin equation over samples of an initial measure p_0 , for example Gaussian, but the convergence may be extremely slow.

The convergence of p_t towards p is defined with a KL divergence

$$KL(p_t, p) = \int p_t(\varphi) \log \frac{p_t(\varphi)}{p(\varphi)} d\varphi \geq 0.$$

De Bruin identity [BBD23] proves that

$$\frac{dKL(p_t, p)}{dt} = -\mathcal{I}(p_t, p), \tag{1}$$

where \mathcal{I} is the relative Fisher information

$$\mathcal{I}(q, p) = \int q(\varphi) \|\nabla_{\varphi} \log \frac{q(\varphi)}{p(\varphi)}\|^2 d\varphi.$$

The exponential convergence of p_t towards p is guaranteed if p satisfies a log-Sobolev inequality, which is recalled.

Definition 2.1. *The log-Sobolev constant $c(p)$ of p is the smallest constant so that for any probability density q*

$$KL(q, p) \leq c(p) \mathcal{I}(q, p). \tag{2}$$

Log-Sobolev constants relate entropy and gradients of smooth normalized functions $f(\varphi)$ in the functional space $\mathbf{L}^2(p d\varphi)$. Indeed, $f^2 = q/p$ satisfies $\|f\|_2 = 1$ in $\mathbf{L}^2(p d\varphi)$ because $\int q(\varphi) d\varphi = 1$, and one can verify that the log-Sobolev inequality (2) is equivalent to

$$\int f^2(\varphi) \log f^2(\varphi) p(\varphi) d\varphi \leq 4 c(p) \int \|\nabla f(\varphi)\|^2 p(\varphi) d\varphi. \tag{3}$$

If p is a normal Gaussian then $c(p) = 1/2$. The log-Sobolev constant gives an exponential rate of convergence of a Langevin diffusion. Indeed, inserting the log-Sobolev definition (2) in (1) proves that

$$KL(p_t, p) \leq e^{-t/c(p)} KL(p_0, p). \tag{4}$$

The time it takes for Langevin diffusions to reach a fixed precision is thus at most proportional to the log-Sobolev constant $c(p)$. The trouble is that $c(p)$ typically grows exponentially with the dimension d of φ .

Upper bounds of the log-Sobolev constant can be computed in two cases [BBD23]. Under independence conditions, if $\varphi = (\varphi_k)_k$ and p can be separated as a tensor product of densities $p(\varphi) = \prod_k p_k(\varphi_k)$ then

$$c(p) = \max_k (c(p_k))_k. \quad (5)$$

In other words, the log-Sobolev constant of independent random variables is the maximum log-Sobolev constant of each variable. The second case, when U is strongly convex, is the Bakry-Emery theorem [BGL⁺14], which proves that

$$\forall \varphi, \nabla_{\varphi}^2 U(\varphi) \geq \alpha Id \Rightarrow c(p) \leq \frac{1}{2\alpha}. \quad (6)$$

The maximum constant α satisfying this equality is the infimum over φ of all eigenvalues of the Hessian matrices $\nabla_{\varphi}^2 U(\varphi)$. The following proposition gives a lower bound of the log-Sobolev constant from the covariance of p .

Proposition 2.1. *Let μ_{\max} be the largest eigenvalue of the covariance of p . The log-Sobolev constant satisfies*

$$c(p) \geq \mu_{\max}/2. \quad (7)$$

This proposition is proved in Appendix E.1. It comes from the inequality between log-Sobolev and Poincaré constants [Led00].

The Langevin diffusion is numerically calculated with an Euler-Maruyama discretization. If $\nabla_{\varphi} U(\varphi)$ is uniformly L -Lipschitz, then the discretization time step can be smaller or equal to L^{-1} [VW22]. Since L is the supremum of all eigenvalues of the Hessians $\nabla_{\varphi}^2 U(\varphi)$, it results from (4) that the number of Langevin diffusion steps to achieve a given precision is proportional to the log-Sobolev constant multiplied by this eigenvalue supremum. It is a normalization of the log-Sobolev constant, which specifies the computational complexity of the Langevin sampling algorithm.

Numerically, the convergence rate of a Langevin diffusion is estimated from the relaxation time τ of the auto-correlation

$$A(t) = \mathbb{E}_{p_{t_0}} \left((\varphi_{t+t_0} - \mathbb{E}[\varphi_{t+t_0}])^T (\varphi_{t_0} - \mathbb{E}[\varphi_{t_0}]) \right) \propto e^{-\frac{t}{\tau}}, \quad (8)$$

for t_0 big enough [Sok91, Sok97]. The relaxation time gives an estimation of the log-Sobolev constant.

To eliminate the bias introduced by the discretization step of Langevin diffusion, synthesis are generated using a Metropolis-Adjusted Langevin Algorithm (MALA) [GM94]. It iterates over discretized Langevin dynamics proposals that are accepted or rejected using the Metropolis-Hastings algorithm.

2.2 Approximation and Learning Gibbs Energies

The Gibbs energy U of a probability density p is usually not known a priori. It is approximated by a parametrized model $p_{\theta} = \mathcal{Z}_{\theta}^{-1} e^{-U_{\theta}}$ where θ is optimized by minimizing $KL(p, p_{\theta})$. Learning θ from a dataset of m samples $\{\varphi^{(i)}\}_{i \leq m}$ is usually done with a maximum likelihood estimation. We shall see that it can be replaced by score matching estimations, which require much fewer calculations, but whose precision depends upon the log-Sobolev constant $c(p)$.

Exponential models We concentrate on linear approximations U_{θ} of the Gibbs energy U , over a family of m' functions $\Phi = \{\phi_k\}_{k \leq m'}$ weighted by $\theta = \{\theta_k\}_{k \leq m'}$

$$U_{\theta}(\varphi) = \theta^T \Phi(\varphi) = \sum_{k \leq m'} \theta_k \phi_k(\varphi). \quad (9)$$

It defines an exponential family of probability densities

$$p_{\theta}(\varphi) = \mathcal{Z}_{\theta}^{-1} e^{-\theta^T \Phi(\varphi)}.$$

A major issue is to find a family Φ providing an accurate approximation U_{θ} of U in high dimension d , despite the curse of dimensionality. In statistics, each ϕ_k is called a moment generating function because the maximum likelihood estimators of θ is specified by the vector of moments $\mathbb{E}_p[\Phi]$ as we shall see. The ϕ_k can be polynomials of φ . However, if we use all high order polynomials of a fixed degree, then the dimension of Φ has a polynomial growth in d . The resulting estimation has a high variance, which requires a large number m of training samples [CCL⁺20]. Markov random fields [GG84] provide a powerful framework where all interactions are supposed to be local over native variables, which defines low-dimensional models. However, it does not apply to data having long-range interactions, which is the case for many image textures [PS00]. In physics, U_{θ} is called an Ansatz. The ϕ_k are considered as interaction potentials. Physical models often rely on multilinear functions of derivatives of φ . The resulting Ansatz are usually local and low-dimensional, but are unable to capture complex systems such as turbulence.

Maximum Likelihood Estimation The next step is to optimize θ in order to best approximate p by p_θ . A maximum likelihood estimator θ maximizes $-\mathbb{E}_p(\log p_\theta)$, which is equivalent to minimize the KL-divergence $KL(p, p_\theta)$. If $U_\theta(\varphi) = \theta^T \Phi(\varphi)$ then this KL divergence is a convex function of θ . The maximum likelihood estimator can thus be calculated with a gradient-descent algorithm of step size ϵ , which computes

$$\theta_{k+1} - \theta_k = \epsilon \left(\mathbb{E}_{p_{\theta_k}}(\Phi) - \mathbb{E}_p(\Phi) \right). \quad (10)$$

The maximum likelihood parameter θ satisfies $\mathbb{E}_{p_\theta}(\Phi) = \mathbb{E}_p(\Phi)$. The resulting p_θ is called a moment projection of p [Bis06]. If the potentials of Φ are linearly independent, then it is uniquely defined if it exists. One can verify that this moment projection is the distribution p_θ which maximizes the entropy $\mathcal{H}(p_\theta) = -\int p_\theta(\varphi) \log p_\theta(\varphi) d\varphi$ subject to the moment condition $\mathbb{E}_{p_\theta}(\Phi) = \mathbb{E}_p(\Phi)$ [Jay57].

The expected value $\mathbb{E}_p(\Phi)$ is estimated from the m samples $\varphi^{(i)}$ with a Monte Carlo sum $m^{-1} \sum_i \Phi(\varphi^{(i)})$. The estimation of $\mathbb{E}_{p_{\theta_k}}(\Phi)$ with a Monte Carlo sum requires computing enough samples of p_{θ_k} . It can be done with a Langevin diffusion, but it requires a considerable amount of computations since it must be run for a sufficiently long time so that the Langevin algorithm converges, and it must be repeated enough so that Monte Carlo sum converges. This is unfeasible if the Langevin convergence rate is too low.

Score Matching Estimation Optimizing $p_\theta = \mathcal{Z}_\theta^{-1} e^{-U_\theta}$ by minimizing the KL divergence is computationally expensive because the gradient descent on θ includes the term $\nabla_\theta \log \mathcal{Z}_\theta = -\mathbb{E}_{p_\theta}(\Phi(\varphi))$. Score matching [HD05] is an appealing alternative. It eliminates the normalization constant \mathcal{Z}_θ by replacing the KL minimization by a minimization of the relative Fisher information, which depends on $\nabla_\varphi \log p$

$$\mathcal{I}(p, p_\theta) = \mathbb{E}_p \left(\frac{1}{2} \|\nabla_\varphi \log p_\theta(\varphi) - \nabla_\varphi \log p(\varphi)\|^2 \right).$$

With an integration by parts, [HD05] proves that it is equivalent to minimize a quadratic loss in θ :

$$\begin{aligned} \ell(\theta) &= \mathbb{E}_p \left(\frac{1}{2} \|\nabla_\varphi U_\theta\|^2 - \Delta_\varphi U_\theta \right) \\ &= \mathbb{E}_p \left(\frac{1}{2} \|\theta^T \nabla_\varphi \Phi(\varphi)\|^2 - \theta^T \Delta_\varphi \Phi(\varphi) \right), \end{aligned} \quad (11)$$

whose solution is obtained without sampling p_θ

$$\theta = M^{-1} \mathbb{E}_p(\Delta_\varphi \Phi(\varphi)) \quad \text{with} \quad M = \mathbb{E}_p(\nabla_\varphi \Phi(\varphi) \nabla_\varphi \Phi(\varphi)^T). \quad (12)$$

Minimizing the score matching loss is thus much faster than a minimization of the KL divergence. Expected values are estimated by an empirical sum over the m samples $\varphi^{(i)}$ of p . Estimation errors introduced by the inversion of M must often be regularized, which is done by adding ϵId to M , where ϵ decreases like m^{-1} for an estimation with m samples.

Score matching is a consistent estimator, which means that if there exists a unique θ^* such that $p = p_{\theta^*} > 0$ then when m goes to infinity, the minimizer θ of the score matching loss converges to θ^* [HD05]. However, the relative precision of a score matching relatively to a maximum likelihood estimation depends on if the KL divergence can be controlled by the relative Fisher information. This is captured by the log-Sobolev constant $c(p)$ defined in (2). For exponential models p_θ , Theorem 2 in [KHR22] bounds the covariance of the score matching estimation with the covariance of the maximum likelihood estimator multiplied by $c(p)^2$. The bound involves a multiplicative constant which also depends upon the regularity of U_θ . Its amplitude can be approximated by the largest eigenvalue squared of the Hessian of U_θ . Similarly to the Langevin diffusion time, the log-Sobolev constant needs to be normalized by this largest eigenvalue amplitude. A score matching thus achieves a comparable accuracy as a maximum likelihood estimator if the number m of samples is multiplied by this normalized log-Sobolev constant, which may be very large.

Multiscale Gaussian and non-Gaussian densities If $p = \mathcal{Z}^{-1} e^{-U}$ is a zero-mean gaussian distribution, then its Gibbs energy is quadratic

$$U(\varphi) = \frac{1}{2} \varphi^T K \varphi \quad \Rightarrow \quad \nabla_\varphi^2 U(\varphi) = K \geq 0. \quad (13)$$

The matrix K is symmetric positive and its inverse $K^{-1} = C$ is the covariance matrix of p . The variance of φ is normalized by imposing that $\text{Trace}(C) = d$. Let μ_{\max} be the largest eigenvalue of C . The Bakry-Emery upper bound of the log-Sobolev constant in (6) together with the lower bounds (7) proves that

$$c(p) = \frac{1}{2} \mu_{\max}. \quad (14)$$

We explained that the number of steps of a Langevin diffusion as well as the inefficiency of score matching relatively to maximum likelihood estimation is proportional to the normalized Sobolev constant, which is multiplied by the supremum of the eigenvalues of $\nabla_\varphi^2 U = K$. It is thus divided by the smallest eigenvalue μ_{\min} of $C = K^{-1}$ and hence proportional to the condition number μ_{\max}/μ_{\min} of the covariance C .

If p is stationary or has stationary increments, then C is diagonalized in the Fourier basis. Multiscale fields have a covariance eigenvalue at each frequency ω which is typically of the order of $|\omega|^{-\eta}$ for some $\eta > 0$ and $\omega \neq 0$. For example, if $K = -\Delta$ then φ is a Brownian motion and $\eta = 2$. The growth of eigenvalues at low frequencies means that φ has long range correlations. In two dimensions, $\pi \geq |\omega| \geq \pi d^{-1/2}$ so $c(p) = \mu_{\max}/2 \propto d^{\eta/2}$ grows with d , which is not modified by the normalization. If p is non-Gaussian then, using proposition 2.1, we still have $c(p) \geq \mu_{\max}/2$ which means that it grows at least like $d^{\eta/2}$. To eliminate the growth due to this bad-conditioning of the covariance, we must separate different frequency bands where eigenvalues have different amplitudes. This is a key idea which motivates hierarchical probability factorization and the renormalization group introduced in the next section.

3 Approximation, Learning and Sampling with Hierarchic Flows

Sampling a probability density p with a Langevin diffusion or estimating its Gibbs energy by score matching becomes unfeasible when the log-Sobolev constant grows with the dimension d . This is typically the case for large multiscale fields φ . This section shows that this difficulty may be avoided if we decompose p into a hierarchic flow of probabilities across scales, and if we renormalize their transition probabilities to bound their log-Sobolev constants.

Section 3.1 reviews multiresolution approximations and wavelet transforms. Section 3.2 explains that a hierarchic flow of probabilities computes an inverse renormalization group studied in [MOBM22]. Sections 3.3 and 3.4 reviews the estimation and sampling of the resulting probability models, with score matching and Metropolis adjusted Langevin diffusions. For stationary probabilities, model parameters satisfy a coupling flow equation given in Section 3.5. Section 3.6 relates wavelet properties to the log-Sobolev constants of transition probabilities.

3.1 Multiresolution Approximations and Wavelets

Multiresolutions define coarse-graining approximations whose evolutions across scales depend upon decomposition coefficients in a wavelet basis [Mal89b, Mey93]. They can be extended to arbitrary data defined on a graph. We begin from the construction of multiresolution approximation on graphs to show that hierarchic flows can be applied to general data structures. We then concentrate on images where we perform numerical experiments.

Multiresolution and wavelets on graphs We consider $\varphi \in \mathbb{R}^d$ defined by its d values $\varphi(n)$ on the nodes of a graph. Multiresolution approximations compute coarse graining approximations of φ of progressively smaller dimensions, by iterating over coarse graining operators [HK22]. Let us write $\varphi_0 = \varphi$. For each $j > 0$, φ_j is calculated from φ_{j-1} with a coarse-graining averaging operator G_j

$$\varphi_j = G_j \varphi_{j-1}. \quad (15)$$

The rows of G_j sum to 1. It is a sparse in matrix which averages groups of neighbor coefficients of φ_{j-1} . The dimension of φ_j is proportional to 2^{-rj} where r is the dimension of the graph. If φ is an image and hence defined on a two-dimensional graph, then $r = 2$. At a level j , each value of φ_j is computed by averaging values of φ_0 over groups of neighbor nodes in the graph, whose sizes are proportional to 2^{rj} . It provides an approximation at the scale 2^j . The graph topology is the prior information allowing to build these multiscale groups. In the simplest cases, the averaged groups are non-overlapping and the coarse graining defines a computational tree [GNC10]. The operator G_j can also be defined as a diagonal operator in the orthogonal basis which diagonalizes the graph Laplacian [HVG11]. It can then be interpreted as a convolution on the graph, which projects φ on the lower-frequency eigenvectors.

The coarse graining is inverted by also computing the high-frequency variations of φ_{j-1} which have been eliminated by the averaging operator G_j . For this purpose, we define a complement operator \bar{G}_j whose rows are sparse with nearly the same support as G_j , and such that $\begin{pmatrix} G_j \\ \bar{G}_j \end{pmatrix}$ is an invertible square matrix. Wavelet coefficients are the high frequencies $\bar{\varphi}_j$ of φ_{j-1} computed by this complement

$$\bar{\varphi}_j = \bar{G}_j \varphi_{j-1}. \quad (16)$$

They measure the variations of φ_{j-1} over local neighborhoods where G_j averages φ_{j-1} . Let (H_j, \bar{H}_j) be the inverse matrix of $\begin{pmatrix} G_j \\ \bar{G}_j \end{pmatrix}$:

$$H_j G_j + \bar{H}_j \bar{G}_j = Id, \quad (17)$$

It results from (15) and (16) that φ_{j-1} can be recovered from $(\varphi_j, \bar{\varphi}_j)$

$$\varphi_{j-1} = H_j \varphi_j + \bar{H}_j \bar{\varphi}_j. \quad (18)$$

If $\begin{pmatrix} G_j \\ \bar{G}_j \end{pmatrix}$ is an orthogonal matrix then $H_j = G_j^T$ and $\bar{H}_j = \bar{G}_j^T$ and this decomposition is orthogonal.

Cascading (G_j, \bar{G}_j) from φ computes a multiscale averaging $\varphi_j = A_j \varphi$ and wavelet coefficients $\bar{\varphi}_j = W_j \varphi$ with

$$A_j = G_j G_{j-1} \dots G_1 \quad \text{and} \quad W_j = \bar{G}_j G_{j-1} \dots G_1. \quad (19)$$

The matrix $W = (A_J, W_J, \dots, W_1)$ is invertible and computes a wavelet transform at all scales. It is orthogonal if each $\begin{pmatrix} G_j \\ \bar{G}_j \end{pmatrix}$ is orthogonal.

Multiresolution of Images Images are sampled on a uniform grid which is a Euclidean graph of dimension $r = 2$. Fast wavelet transforms [Mal89a] are calculated with convolutional and subsampling operators on this graph, which do not depend on j . The operators $G_j = G$ and $\bar{G}_j = \bar{G}$ are defined by

$$G\varphi(n) = \varphi * g(2n) \quad \text{and} \quad \bar{G}\varphi(n) = \varphi * \bar{g}(2n). \quad (20)$$

The filter g is a low-pass filter which averages neighbor pixels in the image. The complement $\bar{g} = (\bar{g}_k)_{1 \leq k \leq 3}$ is composed of 3 separable high-pass filters which compute the image variations over the same neighborhood. The inverse operators H and \bar{H} inserts zeros between each coefficient of φ_j and $\bar{\varphi}_j$ before computing convolutions with dual bi-orthogonal filters h and \bar{h} [Dau92]. This fast wavelet transform is illustrated in Figure 2. Appendix A reviews the properties of conjugate mirror filters (g, \bar{g}) which define an orthogonal matrix $\begin{pmatrix} G \\ \bar{G} \end{pmatrix}$. It implies that $h(n) = g(-n)$ and $\bar{h}(n) = \bar{g}(-n)$. All numerical applications are computed with conjugate mirror filters, but this is not a required condition to define a hierarchic probability flow.

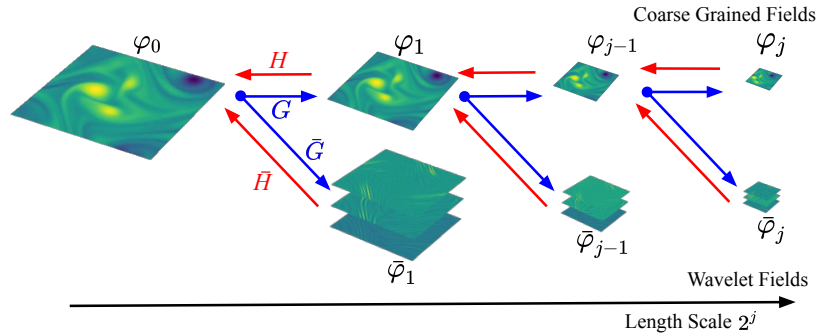


Figure 2: A fast wavelet transform iteratively decomposes an image approximation φ_{j-1} into a coarser approximation φ_j with a sub-sampled low-pass filtering G , and 3 wavelet coefficient images $\bar{\varphi}_j$. They are calculated by \bar{G} with subsampled convolutions with 3 band-pass filters along different orientations. A finer scale image φ_{j-1} is reconstructed from $(\varphi_j, \bar{\varphi}_j)$ with the inverse operator (H, \bar{H}) .

The operators A_j and W_j in (19) are a cascade of j convolutions and sub-samplings by 2. They are thus convolutional operators, followed by a subsampling by 2^j . Coarse-grained images and wavelet coefficients can therefore be written as convolutions with a scaling filter ϕ_j and wavelets $\psi_{j,k}$ subsampled by 2^j :

$$\varphi_j = (\varphi * \phi_j(2^j n))_n \quad \text{and} \quad \bar{\varphi}_j = (\varphi * \psi_{j,k}(2^j n))_{k \leq 3, n}. \quad (21)$$

These scaling filters and wavelets are specified by the filters (g, \bar{g}) as explained in Appendix A. The support width of ϕ_j and $\psi_{j,k}$ is proportional to 2^j . The Fourier transform $\hat{\psi}_{j,k}$ of each wavelet $\psi_{j,k}$ is dilated by 2^{-j} . These Fourier transforms are essentially localized in frequency annuli illustrated in Figure 3(a), around the lower frequencies covered by $\hat{\phi}_j$.

The rows of the wavelet transform $W = (A_J, W_J, \dots, W_1)$ are translated wavelets at all scales, which define a basis of \mathbb{R}^d . It is an orthogonal basis if G and \bar{G} are conjugate mirror filters. To study asymptotic properties of wavelet coefficients when d goes to ∞ , we need to control the convergence of these bases. If we renormalize the support of φ to $[0, 1]^2$ then discrete orthonormal wavelet bases converge to wavelet orthonormal bases of $\mathbf{L}^2([0, 1]^2)$. When the image size d goes to ∞ then normalized discrete wavelets $\psi_{j,k}$ converge to wavelet functions $\psi_{j,k}(x) = 2^{-j} \psi_k(2^{-j} x)$, such that $\{x \mapsto \psi_{j,k}(x - 2^j n)\}_{j \leq 0, n \leq 2^{-j}, k \leq 3}$ is an orthonormal basis of $\mathbf{L}^2([0, 1]^2)$ [Mal09].

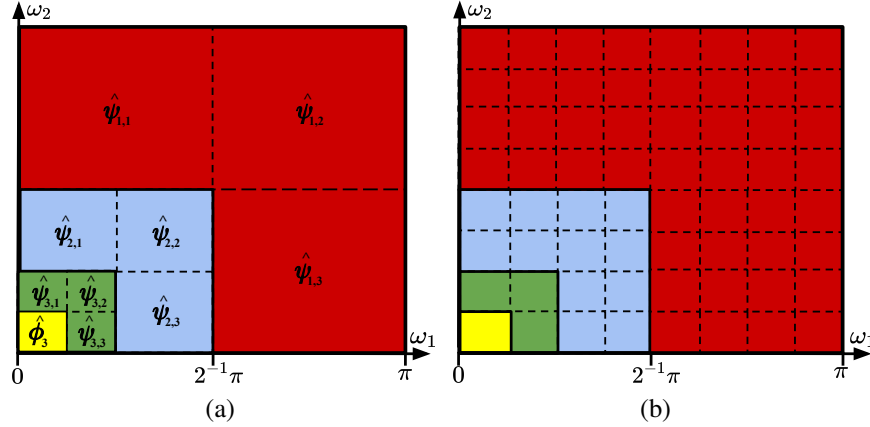


Figure 3: (a): Frequency supports of Fourier transforms of two-dimensional wavelets $\hat{\psi}_{j,k}(\omega_1, \omega_2)$ for $1 \leq k \leq 3$ over 3 scales 2^j . (b): Frequency subdivisions of wavelet packets over a_j levels at each scale 2^j , with $a_1 = 2$, $a_2 = 1$ and $a_3 = 0$.

Wavelet packets The frequency resolution of wavelets can be improved with wavelet packet bases introduced in [CMW92]. A wavelet packets transform sub-decomposes the frequency support of each wavelet. This is done by iteratively applying a_j times the convolutions and subsampling $\begin{pmatrix} G \\ \bar{G} \end{pmatrix}$, after applying \bar{G} to φ_{j-1} . It computes $\bar{\varphi}_j = \bar{G}_j \varphi_{j-1}$ with

$$\bar{G}_j = \begin{pmatrix} G \\ \bar{G} \end{pmatrix}^{a_j} \bar{G}. \quad (22)$$

The matrix $\begin{pmatrix} G \\ \bar{G} \end{pmatrix}$ is orthogonal if $\begin{pmatrix} G \\ \bar{G} \end{pmatrix}$ is orthogonal. It then computes decomposition coefficients in an orthogonal basis of wavelet packet vectors. The filter (22) performs a frequency subdivision of each wavelet frequency band into 2^{2a_j} bands, illustrated in Figure 3(b). These wavelet packets thus have a Fourier transform which are concentrated on square domains, which are 2^{a_j} times more narrow than for wavelets. However, the spatial support of these wavelet packets is 2^{a_j} times larger than for wavelets. Properties of wavelet packets are studied in [CMW92].

3.2 Hierarchic Flows and Renormalization Group

We now consider a random vector φ defined on a graph whose probability density is $p(\varphi)$. If p has a large Sobolev constant, we avoid estimating and sampling p directly. A hierarchic representation of p is defined as a product of conditional probabilities of wavelet coefficients [MOBM22], whose log-Sobolev constants are renormalized through the renormalization of the wavelet coefficients. This hierarchic representation is calculated as an inverse of the renormalization group transformation, which iteratively computes the probability density $p_j(\varphi_j)$ from $p_{j-1}(\varphi_{j-1})$.

Forward renormalisation The renormalization group of Kadanoff [KHY76] and Wilson [Wil71] computes all $p_j(\varphi_j)$ given $p(\varphi)$ at the finest scale. It iteratively computes p_j from p_{j-1} with a marginal integration over the high frequency degrees of freedom, which we represent with the wavelet variables $\bar{\varphi}_j$. Wavelet coefficients $\bar{\varphi}_j$ are normalized by dividing each coordinate $\bar{\varphi}_j(n)$ by its standard deviation $\sigma_{j,i}$. Let $D_j = \text{diag}(\sigma_{j,i}^{-1})_i$ be the corresponding diagonal matrix. Normalizing $\bar{\varphi}_j$ is equivalent to replace \bar{G}_j by $D_j \bar{G}_j$ and \bar{H}_j by $\bar{H}_j D_j^{-1}$.

Since $\varphi_{j-1} = H_j \varphi_j + \bar{H}_j \bar{\varphi}_j$ we have $d\varphi_{j-1} = w_j d\varphi_j d\bar{\varphi}_j$ where $w_j = |\det(H_j, \bar{H}_j)|$ is the Jacobian modulus, and

$$p_j(\varphi_j) = w_j \int p_{j-1}(\varphi_{j-1}) d\bar{\varphi}_j. \quad (23)$$

The use of an appropriate coordinate system to compute the marginal integration of high frequencies $\bar{\varphi}_j$ has been thoroughly studied [De112]. Kadanoff renormalization group [KHY76] computes φ_j from φ_{j-1} with a block averaging, which amounts to define $\bar{\varphi}_j$ as orthogonal wavelet coefficients in the Haar basis, which has a minimal spatial support but is discontinuous. In his first version, Wilson renormalization [Wil71] is computed with Shannon wavelets, whose Fourier transforms have a minimum support but are discontinuous. Shannon wavelets thus have a slow spatial decay. These wavelet properties are reviewed in Appendix A. Other wavelet bases adapted to specific classes of Hamiltonians have been designed by Battle [Bat99], who analyzed relations between the renormalization group and wavelet transforms.

Hierarchic flow as an inverse renormalization If φ_J is of sufficiently low dimension then there is no difficulty to estimate $p_J(\varphi_J)$ from data, or sample this probability density. A hierarchic flow is an inverse renormalization group transformation which maps p_J into p with a Markov chain. It computes $p_{j-1}(\varphi_{j-1})$ by multiplying $p_j(\varphi_j)$ with a conditional probability of φ_{j-1} given φ_j , which is also equal to the conditional density of $\bar{\varphi}_j$ given φ_j

$$p_{j-1}(\varphi_{j-1}) = w_j^{-1} p_j(\varphi_j) \bar{p}_j(\bar{\varphi}_j|\varphi_j). \quad (24)$$

Cascading (24) transforms p_J into p with transition kernels defined by these conditional probabilities

$$p(\varphi) = w^{-1} p_J(\varphi_J) \prod_{j=1}^J \bar{p}_j(\bar{\varphi}_j|\varphi_j) \quad \text{with} \quad w = \prod_{j=1}^J w_j. \quad (25)$$

This inverse wavelet renormalization group [MOBM22] computes p starting from p_J .

3.3 Estimation of a Conditional Probability Model

Given m samples $\{\varphi^{(i)}\}_{i \leq m}$ of p , a model of p is estimated with the hierarchical factorization (25), from exponential models of each conditional probability. Each conditional probability model is estimated from data by score matching, whose precision depends upon its log-Sobolev constant.

Hierarchic model An exponential model p_θ of p is defined from exponential models p_{θ_j} and $\bar{p}_{\bar{\theta}_j}$ of p_J and \bar{p}_j :

$$p_\theta(\varphi) = w^{-1} p_{\theta_J}(\varphi_J) \prod_{j=1}^J \bar{p}_{\bar{\theta}_j}(\bar{\varphi}_j|\varphi_j). \quad (26)$$

An exponential model of p_J is defined as in (9) by

$$p_{\theta_J}(\varphi_J) = \mathcal{Z}_J^{-1} e^{-\theta_J^T \Phi_J(\varphi_J)}. \quad (27)$$

We choose J large enough so that φ_J is sufficiently low-dimensional to easily compute this estimation. For any $j \geq J$, an exponential model of \bar{p}_j is defined by

$$\bar{p}_{\bar{\theta}_j}(\bar{\varphi}_j|\varphi_j) = e^{F_j(\varphi_j) - \bar{\theta}_j^T \Psi_j(\varphi_{j-1})}, \quad (28)$$

where F_j is a free energy which normalizes the conditional probability:

$$\int \bar{p}_{\bar{\theta}_j}(\bar{\varphi}_j|\varphi_j) d\bar{\varphi}_j = e^{F_j(\varphi_j)} \int e^{-\bar{\theta}_j^T \Psi_j(\varphi_{j-1})} d\bar{\varphi}_j = 1. \quad (29)$$

Each free energy F_j is specified by $\bar{\theta}_j$, but it does need to be computed to estimate $\bar{\theta}_j$ or sample $\bar{p}_{\bar{\theta}_j}$.

The model $p_\theta = \mathcal{Z}_\theta^{-1} e^{-U_\theta}$ has a Gibbs energy

$$U_\theta = \theta_J^T \Phi_J + \sum_{j=1}^J (\bar{\theta}_j^T \Psi_j - F_j). \quad (30)$$

Section 3.5 explains that it can be calculated with a coupling flow equation, which requires regressing each F_j .

Score Matching A maximum likelihood estimation computes $\theta = (\theta_J, \bar{\theta}_j)_{j \leq J}$ by minimizing $KL(p, p_\theta)$. It results from the factorization (25) of p and (26) of p_θ that

$$KL(p, p_\theta) = KL(p_J, p_{\theta_J}) + \sum_{j=1}^J \mathbb{E}_{p_j} (KL(\bar{p}_j, \bar{p}_{\bar{\theta}_j})). \quad (31)$$

The minimization of $KL(p, p_\theta)$ is thus obtained by minimizing each $\mathbb{E}_{p_j} (KL(\bar{p}_j, \bar{p}_{\bar{\theta}_j}))$.

As explained in Section 2.2, minimizing a KL divergence with a gradient descent is computationally expensive because it requires computing normalization constants. We thus optimize $\{\theta_J, \bar{\theta}_j\}_j$ by score matching, which replaces the KL divergence by a relative Fisher information. The parameters θ_J are calculated by minimizing the Fisher information $\mathcal{I}(p_J, \bar{p}_{\theta_J})$, which amount to minimize a quadratic loss (11). Interaction parameters $\bar{\theta}_j^T$ are calculated by minimizing the averaged Fisher information

$$\mathbb{E}_{p_j} (\mathcal{I}(\bar{p}_{\bar{\theta}_j}, \bar{p}_j)) = \mathbb{E}_{p_{j-1}} \left(\|\nabla_{\bar{\varphi}_j} \log \bar{p}_j(\bar{\varphi}_j|\varphi_j) - \nabla_{\bar{\varphi}_j} \log \bar{p}_{\bar{\theta}_j}(\bar{\varphi}_j|\varphi_j)\|^2 \right).$$

The score gradient is computed on $\bar{\varphi}_j$ for φ_j fixed, and the Fisher information does not depend on the free energy F_j . Appendix C.1 shows that $\bar{\theta}_j$ is also a solution of a quadratic minimization.

Conditional log-Sobolev constants An upper bound of $\mathbb{E}_{p_j}(KL(\bar{p}_j, \bar{p}_{\bar{\theta}_j}))$ computed from $\mathbb{E}_{p_j}(\mathcal{I}(\bar{p}_j, \bar{p}_{\bar{\theta}_j}))$ depends on a log-Sobolev constant $c(\bar{p}_j)$ averaged over p_j . The conditional log-Sobolev constant $c(\bar{p}_j)$ of $\bar{p}_j(\bar{\varphi}_j|\varphi_j)$ is defined as the smallest constant so that for any conditional probability $\bar{q}(\bar{\varphi}_j|\varphi_j)$

$$\mathbb{E}_{p_j}(KL(\bar{q}, \bar{p}_j)) \leq c(\bar{p}_j) \mathbb{E}_{p_j}(\mathcal{I}(\bar{q}, \bar{p}_j)). \quad (32)$$

One can apply Theorem 2 in [KHR22] to prove that the number m of samples needed for a score matching to achieve a comparable accuracy as a Kullback-Leibler divergence minimization is asymptotically multiplied by this conditional log-Sobolev constant. Section 2.2 shows that for exponential models, minimizing a KL divergence is equivalent to match moments, and hence that minimizing $\mathbb{E}_{p_j}(KL(\bar{p}_j, \bar{p}_{\bar{\theta}_j}))$ is equivalent to find $\bar{\theta}_j$ such that

$$\mathbb{E}_{p_j} \mathbb{E}_{\bar{p}_{\bar{\theta}_j}}(\Psi_j) = \mathbb{E}_{p_{j-1}}(\Psi_j).$$

We can thus evaluate the numerical precision of score matching estimators from this moment matching condition.

3.4 Hierarchic Sampling

A sample φ of a hierarchic model p_θ of p is calculated from coarse to fine scales, by first sampling p_{θ_J} and then iteratively sampling each $\bar{p}_{\bar{\theta}_j}$. These probability densities are sampled with a Metropolis Adjusted Langevin diffusion [GM94, RR98], and we relate the rate of convergence of the unadjusted dynamic to log-Sobolev constants. This is further developed in appendix F.1.

A hierarchic sampling computes a sample φ of p_θ as follows.

- Initialization: compute a sample φ_J of p_{θ_J} .
- For j from J to 1, given φ_j compute a sample $\bar{\varphi}_j$ of $\bar{p}_{\bar{\theta}_j}(\cdot|\varphi_j)$ and set $\varphi_{j-1} = H_j\varphi_j + \bar{H}_j\bar{\varphi}_j$.

The sample $\varphi = \varphi_0$ of p_θ is thus calculated by iterating on a stochastic equation, which recovers φ_{j-1} from φ_j by sampling random high frequencies. The conditional probabilities $\bar{p}_{\bar{\theta}_j}(\cdot|\varphi_j)$ are sampled with a Langevin (or MALA) algorithm, which does not depend upon the normalization free energy F_j .

Convergence of sampling Langevin diffusions has an exponential convergence if their log-Sobolev constants are uniformly bounded. To simplify explanations, we neglect the model approximation error, so $p_{\theta_j} = p_J$ and $p_{\bar{\theta}_j} = \bar{p}_j$.

For a fixed φ_j , a Langevin diffusion approximates $\bar{p}_j(\cdot|\varphi_j)$ by $\bar{p}_{j,t}$ after time t . The product $p_t = w^{-1}p_{J,t} \prod_{j=1}^J \bar{p}_{j,t}$ defines an approximation of p . The KL divergence error between p and p_t can be decomposed as a sum

$$KL(p_t, p) = KL(p_{J,t}, p_J) + \sum_{j=1}^J \mathbb{E}_{p_{j,t}}(KL(\bar{p}_{j,t}, \bar{p}_j)). \quad (33)$$

The decay of $KL(p_{J,t}, p_J)$ is driven by the log-Sobolev constant $c(p_J)$, according to (4). The same result applies to the conditional probabilities \bar{p}_j if we incorporate the expectation in p_j .

Similarly to (4), De Bruin identity (1) implies an exponential convergence of the expected KL divergence:

$$\mathbb{E}_{p_j}(KL(\bar{p}_{j,t}, \bar{p}_j)) \leq e^{-t/c(\bar{p}_j)} \mathbb{E}_{p_j}(KL(p_{j,0}, \bar{p}_j)). \quad (34)$$

Notice that the expected value is in p_j and not in $p_{j,t}$ as in (33) but they converge to the same value because $p_{j,t}$ converges to p_j when t increases.

3.5 Coupling Flow Equation of Stationary Energy Models

In some applications, the Gibbs energy model U_θ in eq. (30) needs to be explicitly calculated. For example, to compute high-dimensional integrals with Monte Carlo reweighing [GRVE22], or to analyze the interaction properties of a physical system. It then requires regressing the free energies F_j over predefined potential vectors. We define hierarchical potentials, allowing to build energy models whose dimensions increase with the field size. This is needed to approximate complex fields having progressively more degrees of freedom when their resolution increases. For stationary probabilities, we prove that U_θ can then be calculated with a discrete coupling flow equation.

Energy calculation Each conditional probability model $\bar{p}_{\bar{\theta}_j}(\bar{\varphi}_j|\varphi_j) = e^{F_j(\varphi_j) - \bar{\theta}_j^T \Psi_j(\varphi_{j-1})}$ involves a free energy $F_j(\varphi_j)$ that is approximated by a linear regression $\alpha_j^T \Phi_j(\varphi_j)$. Inserting this approximation in the energy model (30) gives

$$U_\theta = \theta_J^T \Phi_J + \sum_{j=1}^J (\bar{\theta}_j^T \Psi_j - \alpha_j^T \Phi_j). \quad (35)$$

The coefficients α_j are calculated from the conditional probability normalization (29), up to an additive constant

$$e^{\alpha_j^T \Phi_j(\varphi_j)} \int e^{-\bar{\theta}_j^T \Psi_j(\varphi_{j-1})} d\bar{\varphi}_j \approx cst. \quad (36)$$

Appendix C.2 shows that calculating the gradient along φ_j allows us to compute α_j by minimizing a quadratic form.

Stationary models If $p(\varphi)$ is stationary and hence has a Gibbs energy $U(\varphi)$ which is invariant to translations on the sampling grid of φ then $p_j(\varphi_j)$ is invariant by translation on the coarser sampling grid of φ_j . Hierarchic models in wavelet bases are not strictly stationary because a wavelet orthonormal wavelet basis is not invariant by translations. To define a stationary model, we iteratively project the hierarchic model over translation invariant functions.

Let T_τ be a translation of φ_{j-1} by τ (modulo periodic boundary conditions). A projection of $f(\varphi_{j-1})$ over translation invariant functions of φ_{j-1} is computed by averaging its values over all the translations of φ_{j-1} on its grid \mathcal{G}_{j-1} of size $|\mathcal{G}_{j-1}|$

$$(\text{Ave}_{j-1} f)(\varphi_{j-1}) = \frac{1}{|\mathcal{G}_{j-1}|} \sum_{\tau \in \mathcal{G}_{j-1}} f(T_\tau \varphi_{j-1}). \quad (37)$$

If $f(\varphi_j)$ is a function of $\varphi_j = G\varphi_{j-1}$ then we write $\text{Ave}_{j-1} f = \text{Ave}_{j-1} f_G$ with $f_G(\varphi_{j-1}) = f(G\varphi_{j-1})$. If $f(\varphi_j)$ is invariant to translations of φ_j on its grid \mathcal{G}_j then the sum (37) can be reduced to the 4 translations $\tau \in \mathcal{G}_{j-1}/\mathcal{G}_j$. The following theorem proves that this translation invariant projection of Gibbs energies reduces the Kullback-Leibler error on stationary densities.

Proposition 3.1. *Let $p(\varphi_{j-1})$ be a stationary density. If $q(\varphi_{j-1})$ is a density of energy U and if $\bar{q}(\varphi_{j-1})$ is the density of energy $\text{Ave}_{j-1} U$ then*

$$KL(p, \bar{q}) \leq KL(p, q). \quad (38)$$

The proof is in Appendix E.2. This proposition proves that energy models of stationary probabilities are improved by the projection (37) on translation invariant functions.

Coupling flow equation with hierarchic potentials We introduce hierarchic stationary models where coupling parameters can be calculated with a flow equation from coarse to fine scales, using data to estimate each term. It inverts the renormalization group coupling flow equation, which goes from fine to coarse scales [Del12].

At the largest scale 2^J , we have computed a model U_{θ_J} of the Gibbs energy of p_J . At each scale 2^j , we can compute an approximation $U_{\theta_{j-1}}$ of the Gibbs energy of p_{j-1} from an approximation U_{θ_j} of the Gibbs energy of p_j , by adding the interaction energy model $\bar{\theta}_j^T \Psi_j - \alpha_j^T \Phi_j$ of $\bar{p}_j = p_{j-1}/p_j$. Proposition 3.1 proves that the projection Ave_{j-1} reduces the approximation error. A translation invariant Gibbs energy model having a reduced error is thus

$$U_{\theta_{j-1}} = \text{Ave}_{j-1}(U_{\theta_j} + \bar{\theta}_j^T \Psi_j - \alpha_j^T \Phi_j). \quad (39)$$

The following definition imposes a hierarchic condition on Φ_{j-1} so that θ_{j-1} can be calculated from $(\theta_j, \bar{\theta}_j, \alpha_j)$ with a linear equation.

Definition 3.1. *We say that $\{\Phi_j\}_{0 \leq j \leq J}$ are hierarchic stationary with interactions $\{\Psi_j\}_{1 \leq j \leq J}$ if all $\Phi_j(\varphi_j)$ are invariant to translations of φ_j and if there exists a linear operator Q_j such that*

$$\text{Ave}_{j-1}(\Phi_j, \Psi_j) = Q_j \Phi_{j-1}. \quad (40)$$

This definition generalizes renormalizable models which are self-similar and have the same dimension at all scales. hierarchic stationary potentials are constructed by progressively incorporating new interaction potentials Ψ_j for each j . The dimension of Φ_j is therefore increasing as the scale 2^j decreases. This generalization will allow us to build potential vectors that can approximate energies of complex fields in Section 5.

For hierarchy stationary models, the following proposition derives that the parameter vector θ_{j-1} of $U_{\theta_{j-1}}$ satisfies a linear equation, which relates it to $(\theta_j, \bar{\theta}_j, \alpha_j)$.

Proposition 3.2. *If $\{\Phi_j\}_{j \leq J}$ are hierarchic stationary satisfying (40) then the Gibbs energy $U_{\theta_{j-1}}$ in (39) is given by $U_{\theta_{j-1}} = \theta_{j-1}^T \Phi_{j-1}$ with*

$$\theta_{j-1} = Q_j^T(\theta_j - \alpha_j, \bar{\theta}_{j-1}). \quad (41)$$

Proof. This property is proved by induction on j . It is valid for $j = J$ where $U_{\theta_J} = \theta_J^T \Phi_J$. Suppose that it is valid for $j \geq J$. Inserting $U_{\theta_j} = \theta_j^T \Phi_j$ in (39) implies with (40) that

$$U_{\theta_{j-1}} = (\theta_j - \alpha_j, \bar{\theta}_j)^T (\Phi_j, \Psi_j) = \theta_{j-1}^T \Phi_{j-1},$$

where θ_{j-1} satisfies (41). □

This proposition computes energy models with a discrete coupling flow equation in a wavelet basis, from coarse to fine scales. It inverts the renormalization group equation, which goes from fine to coarse scale. In a Fourier basis, this renormalization group equation can be written as a differential equation, which defines a Polchinski flow [Pol84, BBD23]. The inverse equation involves the parameters of conditional probabilities, which specifies fine scale probabilities from coarser scales. The dimension of the coupling flow vector θ_j also increases as the scale decreases, which is necessary to obtain accurate models of complex fields which are not exactly self-similar. At the finest scale $j = 0$, we obtain a translation invariant Gibbs energy $U_{\theta_0} = \theta_0^T \Phi_0$ of a stationary model p_{θ_0} of $p = p_0$.

3.6 Log-Sobolev Constants and Wavelet Choice

We want to decompose p having a large log-Sobolev constant into conditional probabilities \bar{p}_j having smaller log-Sobolev constants, which can therefore be learned and sampled more easily. To do so, we study the choice of basis and of the hierarchical projectors G_j and \bar{G}_j . In the following, we suppose that $\begin{pmatrix} G_j \\ \bar{G}_j \end{pmatrix}$ is an orthogonal matrix.

Selection of eigenvectors The Bakry-Emery theorem gives an upper bound of $c(\bar{p}_j)$ from the inverse of the smallest eigenvalue of the Hessians $\nabla_{\bar{\varphi}_j}^2 \bar{U}_j$, if it is positive. This suggests choosing G_j and \bar{G}_j so that it maximizes this minimum eigenvalue. In the orthogonal case, $\varphi_{j-1} = \bar{G}_j^T \bar{\varphi}_j + G_j^T \varphi_j$ so

$$\nabla_{\bar{\varphi}_j}^2 \bar{U}_j = \bar{G}_j (\nabla_{\varphi_{j-1}}^2 U_{j-1}) \bar{G}_j^T. \quad (42)$$

The Hessian eigenvalues of \bar{U}_j are thus obtained by selecting the Hessian eigenvalues of U_{j-1} with the orthogonal operator \bar{G}_j . To minimize the log-Sobolev constant, \bar{G}_j must eliminate small or negative eigenvalues of $\nabla_{\varphi_{j-1}}^2 U_{j-1}(\varphi_{j-1})$. If the high amplitude eigenvectors of $\nabla_{\varphi_{j-1}}^2 U_{j-1}(\varphi_{j-1})$ are concentrated in a fixed linear space with high probability, then the range of \bar{G}_j^T should be included in this space.

Renormalized log-Sobolev lower-bound The renormalization of $\bar{\varphi}_j$ by D_j aims at preconditioning the covariance of \bar{p}_j to avoid creating a large log-Sobolev constant. If $\bar{\mu}_{\max,j}$ is the largest eigenvalue of the covariance \bar{C}_j of $\bar{\varphi}_j$ then (7) proves that

$$c(\bar{p}_j) \geq \frac{1}{2} \bar{\mu}_{\max,j}. \quad (43)$$

If p is Gaussian then $\bar{p}_j(\cdot|\varphi_j)$ is then also Gaussian so $c(\bar{p}_j) = \bar{\mu}_{\max,j}/2$. The log-Sobolev normalization amounts to multiply by the largest eigenvalue of $\nabla_{\bar{\varphi}_j}^2 \bar{U}_j$. In the Gaussian case it divides by the smallest eigenvalue of the covariance and is thus equal to the covariance condition number. The covariance C_j of φ_j is computed iteratively from C_0 with (15), which implies that $C_j = G_j C_{j-1} G_j^T$. The covariance \bar{C}_j of $\bar{\varphi}_j$ is computed from \bar{G}_j , which includes the renormalization. It gives

$$\bar{C}_j = \bar{G}_j C_{j-1} \bar{G}_j^T \quad \text{with} \quad \text{diag}(\bar{C}_j) = Id. \quad (44)$$

The covariance C_{j-1} is projected and renormalized by \bar{G}_j , which sets the diagonal values of \bar{C}_j to 1. The maximum eigenvalue and the condition number of \bar{C}_j do not grow with the dimension d if \bar{G}_j represents C_{j-1} over a basis of nearly eigenvectors, so that all eigenvalues remain of the order of 1. This necessary condition to control the log-Sobolev constant is not sufficient. Non-convex Gibbs energies may have much larger log-Sobolev constants. This issue is studied numerically in Sections 4.2 and 5.2 for scalar potential energies and 2d turbulence data.

Choice of wavelet and wavelet packet basis For multiscale stationary processes, we explain that the largest eigenvalues and the condition numbers of all \tilde{C}_j remain bounded if the wavelet has a Fourier transform which is sufficiently well localized. We do not give mathematical details but quote the main results. It gives necessary conditions to control the growth of $c(\bar{p}_j)$ and its normalization, with the dimension d .

Multiscale stationary fields have a density p whose covariance is diagonalized in a Fourier basis, with eigenvalues which grow like $|\omega|^{-\eta}$ at low-frequencies. In an image of width $d^{1/2}$, if the smallest eigenvalue is of the order of 1 then the largest eigenvalue is of the order of $d^{\eta/2}$, which implies that the log-Sobolev constant $c(p)$ increases at least like $d^{\eta/2}$. A hierarchical factorization tries to avoid this growth by renormalizing $\bar{\varphi}_j$ so that the normalized log-Sobolev constant remains bounded for all d . A necessary condition is that the condition number of the normalized covariance of $\bar{\varphi}_j$ does not grow with d . Computing this condition number when d goes to infinity amounts to study the decomposition of the limit covariance operator of φ in a wavelet orthonormal basis of $\mathbf{L}^2([0, 1]^2)$, by normalizing the maximum to 1.

The renormalization sets the diagonal of \tilde{C}_j to 1 so that its lowest and largest eigenvalues remain of the order of 1. It is valid if the covariance is preconditioned by its diagonal in the wavelet basis. Classes of linear singular operators, preconditioned by their diagonal in a wavelet basis, have been thoroughly studied in harmonic analysis [Mey93]. It is used to prove that such bases are unconditional bases of Sobolev, Holder and Besov spaces. Preconditioning in wavelet bases is also applied to the fast resolution of elliptic problems [Jaf92]. For appropriate wavelets, it is valid for large classes of pseudo-differential operators, and for singular homogeneous operators diagonalized in a Fourier basis with eigenvalues proportional to $|\omega|^{-\eta}$. It requires that the Fourier transform of wavelets are sufficiently well localized.

At low frequencies, each wavelet ψ_k must have a Fourier transform $\hat{\psi}_k$ satisfying $|\hat{\psi}_k(\omega)| = O(|\omega|^{\eta/2})$, to avoid being contaminated by the explosion of the largest eigenvalues at low-frequencies. If a wavelet has m vanishing moments, then Appendix A shows that $|\hat{\psi}_k(\omega)| = O(|\omega|^m)$. We thus choose a wavelet with $m \geq \eta/2$ vanishing moments. At high frequencies, $|\hat{\psi}_k(\omega)|$ must have a decay faster than $|\omega|^{-\eta/2}$, which is satisfied if ψ_k has $m \geq \eta/2$ derivatives in $\mathbf{L}^2([0, 1]^2)$. If the ψ_k have a compact support, more than $\eta/2$ vanishing moments and $\eta/2$ bounded derivatives, then one can prove [Mey93, MOBM22] that the maximum eigenvalue and the condition number of the covariance of all $\bar{\varphi}_j$ are uniformly bounded for all j and d .

A bad conditioning may be produced by the smallest eigenvalues of the covariance, which are properly renormalized if they have a decay which is faster than a power law at the highest frequencies. At high frequencies, the frequency resolution of wavelets is not sufficient to follow this fast decay and thus renormalize these small eigenvalues. To ensure that the condition number of the covariance does not increase with d , one can represent the high-frequency $\bar{\varphi}_j$ in a wavelet packet basis having a better frequency resolution. Each wavelet packet must have a Fourier transform concentrated in a sufficiently narrow frequency domain, where the covariance eigenvalues vary by a limited multiplicative factor. The frequency width of these wavelet packets is 2^{a_j} times more narrow than wavelets if computed with a wavelet packet filter \tilde{G}_j defined in (22). The constant a_j is adjusted to define wavelet packet coefficients $\bar{\varphi}_j$ whose normalized covariance \tilde{C}_j has a condition number of the order of 1. Improving wavelet packet frequency resolutions by 2^{a_j} also increases their spatial support by a factor 2^{a_j} . We thus choose a_j to be as small as possible. This is applied in Section 5.2 to improve the Langevin mixing time for 2D turbulence vorticity fields.

4 Hierarchical Models of Local Scalar Potentials

Scalar potential models introduced in this section are local interaction models often used in statistical physics. We study the particular case of the φ^4 model to illustrate the estimation and sampling properties of hierarchical probability flows at phase transitions.

4.1 Scalar potential energies and φ^4 model

Physical systems at equilibrium have a probability density $p = \mathcal{Z}^{-1} e^{-U}$ with an energy U decomposed in a quadratic term corresponding to two point interactions and a non-linear potential $V(\varphi)$ which specifies all other interactions:

$$U(\varphi) = \frac{-\beta}{2} \varphi^T \Delta \varphi + V(\varphi). \quad (45)$$

The Laplacian Δ is discretized over the grid of φ and defines the kinetic energy at a temperature $1/\beta$. Some physical systems [Ram20] have a potential V which is reduced to a sum of scalar potentials at all locations n

$$V(\varphi) = \sum_n v(\varphi(n)). \quad (46)$$

It enforces no interactions between different sites n but favors values of $\varphi(n)$ where v is nearly minimum. Ferromagnetism and second order phase transitions are captured by the φ^4 model [ZJ21]. Its scalar potential $v(t) = t^4 - (1+2\beta)t^2$ is non-convex, with a double-well which pushes the values of each $\varphi(n)$ towards $+1$ or -1 [ZJ21].

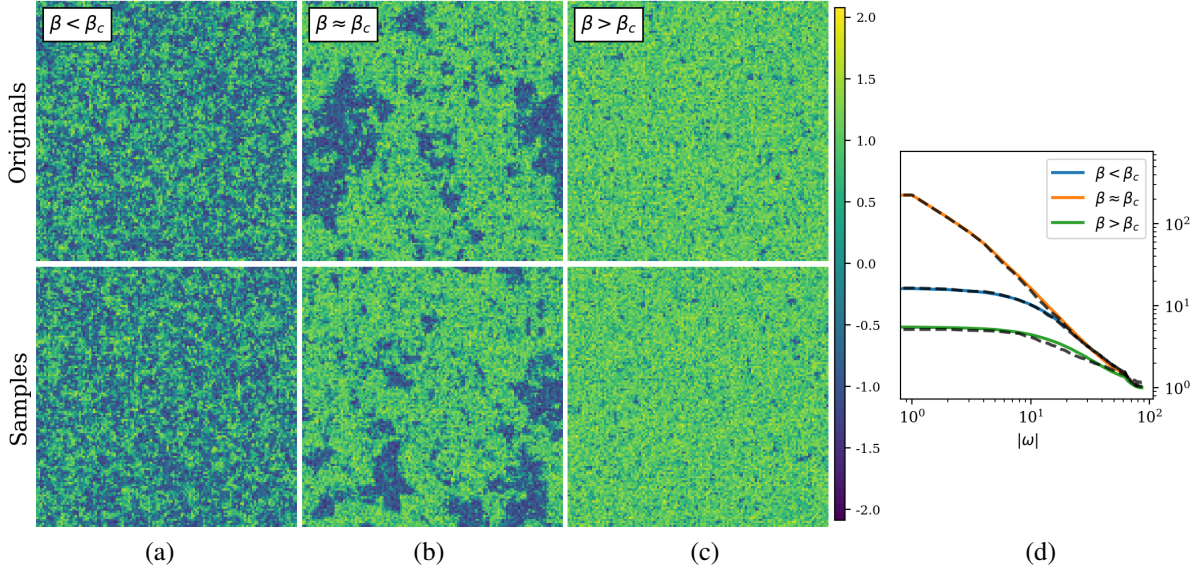


Figure 4: Top Row : Realizations of φ^4 fields at temperature $1/\beta$, and system size $d = 128^2$. (a): For $\beta = 0.5 < \beta_c$, the system is disordered with short range correlations. (b): At the phase transition, $\beta = 0.68 \approx \beta_c$, the field is self-similar, with long range correlations. (c): For $\beta = 0.76 > \beta_c$, the system is in a ferromagnetic phase, with a non-zero mean (here positive). Bottom row: samples generated with a hierarchic factorization in a Haar wavelet basis with the same β in (a,b,c). (d) : The graph shows the covariance eigenvalues (power spectrum) in these 3 cases, as a function of the two-dimensional frequency radius $|\omega| = (|\omega_1|^2 + |\omega_2|^2)^{1/2}$. For $\beta = \beta_c$, eigenvalues have a power-law decay and develop a singularity at low frequencies, which correspond to long-range correlations. We superimposed in dashed line the covariance eigenvalues of a hierarchic model estimated by score matching. For visualization, the spectrum at different temperatures are multiplied by a constant which aligns their minimum eigenvalue.

If $\beta = 0$ then $U(\varphi) = \sum_n v(\varphi(n))$. Each $\varphi(n)$ are then i.i.d independent random variables of density $\tilde{p}(t) = \eta e^{-v(t)}$. The power spectrum is constant. We saw in (5) that the independence implies that the log-Sobolev constant satisfies $c(p) = c(\tilde{p})$, and thus does not depend upon the dimension of φ . If $\beta > 0$ the Laplacian correlate pixels over a progressively larger neighborhood as β increases. It increases the power spectrum at low frequencies. In the thermodynamic limit $d \rightarrow \infty$ of infinite system size, the φ^4 energy has a phase transition at $\beta_c \approx 0.68$ [KMR16]. The power spectrum then has a power $|\omega|^{-\eta}$ with $\eta = 1.75$ as shown in Figure 4(d). It is singular at low-frequencies, which corresponds to a field having long range correlations. Figure 4 shows realizations of φ^4 fields for $\beta < \beta_c$, $\beta = \beta_c$ and $\beta > \beta_c$. For $\beta > \beta_c$ (low-temperature), there are two phases where the average field value is strictly positive or strictly negative, which explains ferromagnetism. Figure 4(d) corresponds to one phase where most field values are close to 1.

Hessians eigenvalues The probability density p has a non-convex energy U whose Hessian is

$$\nabla_{\varphi}^2 U(\varphi) = -\beta \Delta + \text{diag}(\mu_n)_n \quad \text{with} \quad \mu_n = v''(\varphi(n)).$$

The Laplacian Δ is diagonal in the Fourier basis with eigenvalues $|\omega|^2$. The scalar potential is diagonal in a Dirac basis with positive and negative eigenvalues. These eigenvalues are much larger than the Laplacian eigenvalues at low-frequencies and produce eigenvectors of the Hessian $\nabla_{\varphi}^2 U$ having negative eigenvalues.

To define a hierarchic model with conditional probabilities $\tilde{p}_j(\tilde{\varphi}_j|\varphi_j)$ having small log-Sobolev constants, Section 3.6 explains that we may choose projectors \tilde{G}_j that select eigenvectors having high amplitude positive eigenvalues, and discard negative eigenvalues. At the finest scale, this can be done [GLBM23] with a first high-frequency filter \tilde{G}_1 which eliminates low frequencies and selects high-frequency variables $\tilde{\varphi}_1$. The resulting interaction energy \tilde{U}_1 has a projected Hessian

$$\nabla_{\tilde{\varphi}_1}^2 \tilde{U}_1(\varphi) = -\beta \tilde{G}_1 \Delta \tilde{G}_1^T + \tilde{G}_1 (\text{diag}(\mu_i)_i) \tilde{G}_1^T.$$

Figure 5(a) compares the histograms of the eigenvalues of $\nabla_{\varphi_0}^2 U_0$ and the Hessian $\nabla_{\bar{\varphi}_1}^2 \bar{U}_1$ (without normalization for comparison purposes). It is computed with a Symlet-4 wavelet for φ^4 at critical temperature $\beta = \beta_c$. As expected, $\nabla_{\bar{\varphi}_1}^2 \bar{U}_1$ has fewer negative eigenvalues than $\nabla_{\varphi_0}^2 U_0$, but some still remain. These negative eigenvalues can be almost everywhere eliminated by an orthogonal \bar{G}_1 selecting a more narrow high-frequency band than wavelets. This can be done with wavelet packets [GLBM23]. Since φ^4 has a self-similar probability distribution at the phase transition $\beta = \beta_c$, the same result is obtained at all other scales 2^j .

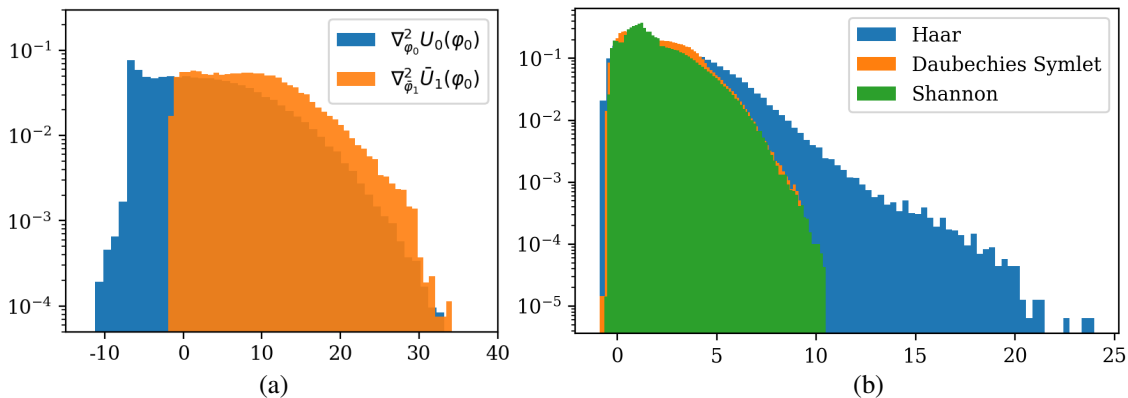


Figure 5: (a): We consider images φ_0 of the φ^4 model of dimension $d = 128^2$, for a critical $\beta = \beta_c$. The approximations φ_1 are calculated with a Symlet-4 filter at the finest scale 2^1 . The graph shows the distributions of eigenvalues of the Hessian $\nabla_{\varphi_0}^2 U_0$ in blue, and of $\nabla_{\bar{\varphi}_1}^2 \bar{U}_1 = \nabla_{\bar{\varphi}_1}^2 U_0$ (without renormalization) in orange. The most negative eigenvalues of $\nabla_{\varphi_0}^2 U_0$ correspond to low frequency eigenvectors. They do not appear in $\nabla_{\bar{\varphi}_1}^2 \bar{U}_1$. (b): Distributions of eigenvalues of Hessians $\nabla_{\bar{\varphi}_j}^2 \bar{U}_{\theta_j}$ at all scales $2^j \leq 2^J$, for $d = 32^2$, with $J = 3$, for samples of hierarchic models of φ^4 at phase transition. They are computed for Haar (blue), Symlet-4 (orange) and Shannon wavelets (green). Eigenvalues are more concentrated when the wavelet has a better frequency localization.

Figure 5(b) displays the distribution of eigenvalues of $\nabla_{\bar{\varphi}_j}^2 \bar{U}_{\theta_j}(\varphi_{j-1})$, for samples φ_{j-1} of a hierarchic model, computed at all scales $2^j \leq 2^J$. These distributions are calculated for hierarchic factorization computed with Haar (*blue*), Symlet-4 (*orange*) and Shannon (*green*) wavelets. The Hessian eigenvalues are nearly the same for Shannon wavelets and Symlet-4. For Haar wavelets there are much more high amplitude eigenvalues. Indeed, Haar wavelets are not as well localized in frequency. For a Haar wavelet, $|\hat{\psi}(\omega)|^2$ decays like $|\omega|^{-2}$ at high frequencies because $\psi(x)$ is discontinuous. The high amplitude eigenvalues are due to this slow high-frequency decay, which slowly compensate for the growths of the Hessian eigenvalues proportional to $|\omega|^\eta$ for $\eta = 1.75$ [Täu14].

The existence of negative Hessian eigenvalues prevents using the Bakry-Emery theorem to compute an upper bound on the log-Sobolev constant of wavelet conditional probabilities. However, we shall see in the next section that these remaining negative eigenvalues do not prevent the Langevin diffusion from exponential convergence, even at the phase transition. These numerical results are an indication that log-Sobolev constant of wavelet conditional probabilities do not depend upon the scale.

4.2 Learning and Sampling hierarchic Scalar Potential Energies

This section reviews the estimation of hierarchic models of scalar potentials introduced in [MOBM22], and its application to the estimation and sampling of the φ^4 model at critical temperature. It is shown in [MOBM22] that the critical slowing down disappears when sampling the conditional probabilities of a hierarchic factorization, although the Hessians still have negative eigenvalues in Figure 5. We compare different wavelets for learning and sampling the φ^4 model at critical temperature. We shall see that the model errors decrease by decreasing the wavelet support. Learning precision versus sampling convergence introduces a trade-off between spatial and frequency localization, which justifies the use of wavelets as opposed to a Fourier basis, and where Haar wavelets are the winners.

Hierarchic scalar potentials A hierarchic model is defined with a coarse scale model $U_{\theta_j} = \theta_j^T \Phi_j$ and interaction energy models $\bar{U}_{\bar{\theta}_j} = \bar{\theta}_j^T \Psi_j$ at each scale $2^j \geq 2^J$. We define Φ_j and each Ψ_j for scalar potential energies, and prove that it defines a stationary hierarchic model, whose coupling parameters are computed with a coarse to fine coupling flow equation.

At the coarsest scale, $U_{\theta_J} = \theta_J^T \Phi_J$ includes a two-point interaction matrix and a parametric scalar potential

$$\theta_J^T \Phi_J(\varphi_J) = \frac{1}{2} \varphi_J^T K_J \varphi_J + V_{\gamma_J}(\varphi_J), \quad (47)$$

where $V_\gamma(\varphi)$ has a scalar potential $v_\gamma(t) = \sum_k \gamma_k \rho_k(t)$ decomposed over a finite approximation family $\{\rho_k(t)\}_k$ with coefficients $\gamma = (\gamma_k)_k$. It results that

$$V_\gamma(\varphi) = \gamma^T \Gamma(\varphi) \quad \text{with} \quad \Gamma(\varphi) = \left(\sum_n \rho_k(\varphi(n)) \right)_k. \quad (48)$$

We use translated sigmoids which do not grow at infinity: $\rho_k(t) = (1 + \exp((t - t_\ell)/\sigma_k))^{-1}$. In numerical calculations there are 40 evenly spaced translations t_k , on the support of the distribution of each $\varphi_J(n)$, and $\sigma_k = \frac{3}{2}(t_{k+1} - t_k)$. To define a model of p_J which is stationary is equivalent to impose that K_J is a convolutional operator.

The interaction Gibbs energy $\bar{U}_{\bar{\theta}_j}$ of $p_j(\bar{\varphi}_j|\varphi_j)$ includes two-point interactions within the high frequencies $\bar{\varphi}_j$, between high frequencies $\bar{\varphi}_j$, and the lower frequencies φ_j , with convolution matrices \bar{K}_j and \bar{K}'_j , plus a scalar potential

$$\bar{U}_{\bar{\theta}_j}(\varphi_{j-1}) = \bar{\varphi}_j^T \bar{K}_j \bar{\varphi}_j + \bar{\varphi}_j^T \bar{K}'_j \varphi_j + \bar{V}_{\bar{\gamma}_j}(\varphi_{j-1}) = \bar{\theta}_j^T \Psi_j(\varphi_{j-1}). \quad (49)$$

It defines

$$\bar{\theta}_j = \begin{pmatrix} \bar{K}_j \\ \bar{K}'_j \\ \bar{\gamma}_j \end{pmatrix} \quad \text{and} \quad \Psi_j(\varphi_{j-1}) = \begin{pmatrix} \bar{\varphi}_j \bar{\varphi}_j^T \\ \bar{\varphi}_j \varphi_j \\ \Gamma(\varphi_{j-1}) \end{pmatrix}. \quad (50)$$

The stationary interaction \bar{K}'_j between high and low-frequencies has an energy contribution which is typically much smaller than the interaction \bar{K}_j within high frequencies, because φ_j and $\bar{\varphi}_j$ are computed over frequency domains having a small overlap. The following theorem defines a stationary hierarchic model from this scalar potential interactions Ψ_j . With an abuse of notation, we write $\varphi * \varphi^T$ the convolution between φ and $\varphi^T(n) = \varphi(-n)$. We recall from (65) that $\varphi_j(n) = \varphi * \phi_j(2^j n)$.

Theorem 4.1. *For any $j \geq J$,*

$$\Phi_j(\varphi_j) = \begin{pmatrix} \varphi_j * \varphi_j^T \\ \Gamma(\varphi_j * \phi_\ell) \end{pmatrix}_{J-j \geq \ell \geq 0} \quad (51)$$

defines stationary hierarchic potentials with interactions Ψ_j in (49). Regressing each free energy F_j over Φ_j defines a fine scale Gibbs stationary model for $j = 0$

$$U_\theta(\varphi) = \frac{1}{2} \varphi^T K \varphi + \sum_{j=0}^J V_j(\varphi) \quad \text{with} \quad V_j(\varphi) = \gamma_j^T \Gamma(\varphi * \phi_j), \quad (52)$$

where K is a convolution matrix and $(\gamma_j)_{0 \leq j \leq J}$ are scalar potential parameters computed by a coupling flow equation.

The proof is in Appendix E.3. At each scale 2^j , this Gibbs energy has a different scalar potential $V_j(\varphi) = \gamma_j^T \Gamma(\varphi * \phi_j)$. The convolution with ϕ_j averages φ over a domain proportional to 2^j . As the scale 2^j increases, it becomes more and more non-local. Scalar potential energies (45), such as the φ^4 model, have a single potential $V_0(\varphi) = \sum_n v_0(\varphi(n))$ at the finest scale $j = 0$ and are thus local. They correspond to a particular case where $\gamma_j = 0$ for $j < 0$. However, a single fine scale scalar potential is not always sufficient. This is the case of cosmological weak-lensing fields, which can be approximated by incorporating different scalar potentials V_j at different scales. In this case, numerical results show that hierarchic scalar potential models provide accurate approximations of U [GLBM23, MOB22].

Hierarchic model estimation and sampling The parameters $\{\theta_J, \bar{\theta}_j\}_{j \leq J}$ are estimated from m samples $\{\varphi^{(i)}\}_{i \leq m}$ of p , with the conditional score matching algorithm of Section 3.3. Samples φ of $p_\theta = w^{-1} p_{\theta_J} \prod_j \bar{p}_{\bar{\theta}_j}$ are computed with the hierarchical sampling algorithm of Section 3.4, which does not require the knowledge of the free energies, or normalizations, of the $\bar{p}_{\bar{\theta}_j}$. The MALA algorithm includes a rejection of Langevin diffusion propositions. The scalar potential also rejects proposals outside a high probability interval. Figure 4 compares original samples from p computed with exact φ^4 energies at different temperatures, and samples of a hierarchical model \bar{p}_θ estimated in a Haar wavelet basis. Generated images have textures which cannot be distinguished visually from the original image textures.

The model precision can be evaluated by computing the resulting stationary energy and by comparing it with the true φ^4 energy. A hierarchic stationary model (52) of φ^4 is calculated in the Haar basis from the estimated interaction energy

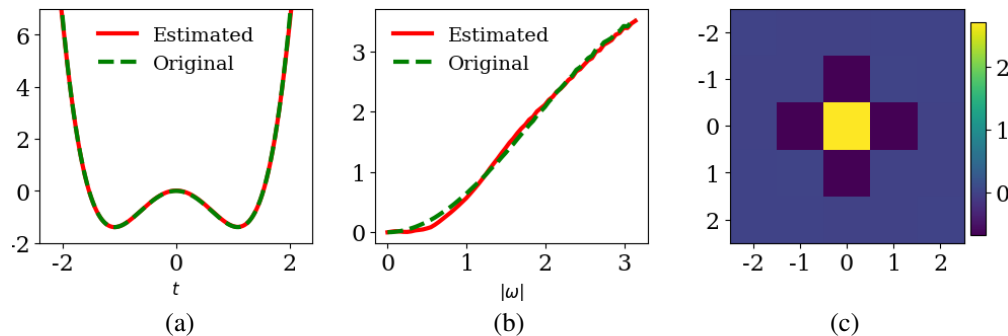


Figure 6: Original and estimated energy of φ^4 at critical temperature, for images of size $d = 128 \times 128$. (a): Superposition of the scalar potential $v(t)$ of the φ^4 model for $\beta = \beta_c$ and the estimated scalar potential $v_0(t)$ of the hierarchical stationary energy model U_θ . (b): Superposition of the Laplacian eigenvalues (in the Fourier basis) and the eigenvalue of the estimated 2-point interaction matrix K of U_θ . (c): Estimated convolution kernel of K . These results show that the hierarchical stationary model calculated in a Haar basis gives a precise approximation of the φ^4 energy.

parameters $\bar{\theta}_j$ and the free energy parameters α_j . The only non-zero scalar potential is at the finest scale $j = 0$. It implies that the scalar potential of the free energy F_j cancels the scalar potential of the energy at the previous scale. Figure 6 compares the estimated energy U_θ and original φ^4 energy. Figure 6(a) compares the estimated $v_0(t)$ and original scalar potential function $v(t)$. Figure 6(b) compares the eigenvalues of the estimated two-point interaction matrix K and of a Laplacian, which are the two-point interactions of the φ^4 model. Figure 6(c) shows that the convolution kernel of K is indeed close to a Laplacian. It shows that the hierarchical stationary model in a Haar wavelet basis gives an accurate approximation of the φ^4 energy model at the phase transition. We shall see at the end of this section that the estimation error becomes larger with Daubechies and Shannon wavelets, which have a spatial support larger than Haar wavelets.

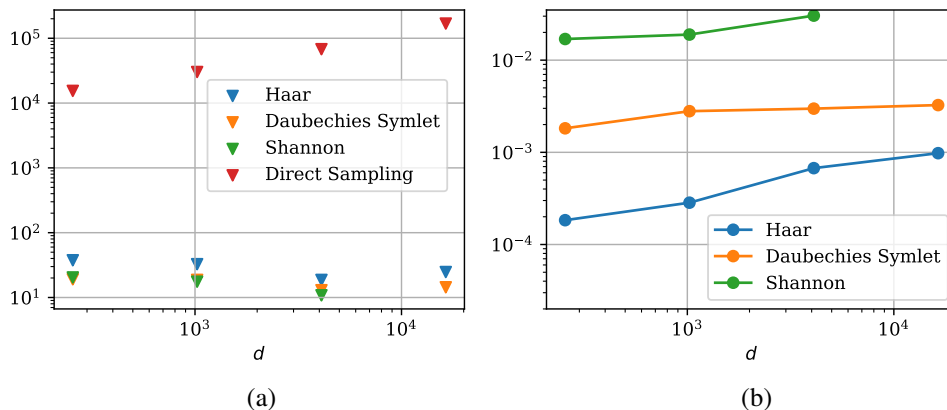


Figure 7: (a): Normalized Langevin auto-correlation relaxation time of the φ^4 model at critical temperature and for hierarchical models computed in different wavelet bases. In red is shown the normalized relaxation time of a Langevin applied directly on the energy of the φ^4 model, which grows with the image dimension d . It illustrates the critical slowing down. On the contrary, it remains constant for all wavelet hierarchical models. This constant depends upon the log-Sobolev constant of wavelet conditional probabilities, which depends upon the wavelet choice. It is maximum for Haar and smaller for Daubechies-4 Symlet and Shannon wavelets.

(b): Approximation error of hierarchical models computed in the same bases as in (a). This error measures the difference between the marginal and second order moments of samples of φ^4 and the same moments computed from samples of hierarchical models in each wavelet basis. It is quantified with a KL divergence calculated in (84). The error decreases when the wavelet support decreases because it is dominated by the estimation error of the non-convex scalar potential. It is much smaller for a Haar wavelet than for Symlet-4 wavelets. The Shannon wavelet which has a non-compact support with a slow spatial decay yields a much larger error than Haar and Symlet-4 wavelets.

Critical slowing down at phase transition Sampling $p = \mathcal{Z}^{-1} e^{-U}$ with an undajusted Langevin algorithm has a computational complexity proportional to the number of iterations after discretization. It is proportional to the log-Sobolev constant $c(p)$ multiplied by the largest eigenvalue of the Hessian of U , as explained in Section 2.1. For $\beta = \beta_c$, it suffers from a critical slowing down due to a growth of the log-Sobolev constant when the system size d increases. The convergence of Langevin diffusion is estimated by the auto-correlation relaxation time defined in (8), which is typically proportional to the log-Sobolev constant $c(p)$. The computational complexity is evaluated by the normalized relaxation τ equal to auto-correlation relaxation time divided by the discretisation time step. Figure 7(a) gives the evolution of this normalized hierarchic relaxation time τ as a function of the system size d for $\beta = \beta_c$. It grows like $d^{\eta_0/2}$ for $\eta_0 = 2$ [Pod96, Set21, Täu14]. This behavior is partly explained by the log-Sobolev lower-bound $c(p) \geq \mu_{\max}/2$ where μ_{\max} is the largest eigenvalue of the covariance. It grows like $d^{1.75/2}$ for $\beta = \beta_c$, as shown by the power spectrum in Figure 4. However, this explanation is not complete since the covariance is only a lower-bound. The log-Sobolev constant has a faster growth exponent where 1.75 is replaced by 2 which gives d . Indeed, it also suffers from the non-convexity of the scalar potential, which is not captured by the covariance lower-bound.

It has been shown in [MOBM22] that a hierarchical factorization in a wavelet basis avoids this critical slowing down. To compute the normalized auto-correlation relaxation time of the hierarchical sampling algorithm, we compute for each j the relaxation time $\bar{\tau}_j$ of probability $p_{\bar{\varphi}_j}(\varphi_j|\varphi_j)$, like in (8). The hierarchic normalized auto-correlation relaxation time τ , is defined by

$$\tau = \sum_{j=1}^J \frac{\bar{d}_j}{d} \bar{\tau}_j + \frac{d_J}{d} \tau_J, \quad (53)$$

where (\bar{d}_j, d_j) are the dimensions of $(\bar{\varphi}_j, \varphi_j)$. Appendix F.1 explains how to estimate the relaxation time of each conditional probability. Each normalized relaxation time $\bar{\tau}_j$ is divided by the discretization time-step. To evaluate the overall computational complexity, each $\bar{\tau}_j$ is multiplied by the relative size \bar{d}_j/d of the gradient $\nabla_{\bar{\varphi}_j} \bar{U}_{\bar{\varphi}_j}$.

Figure 7(a) gives the hierarchic normalized auto-correlation relaxation time, depending on the system size d , for different wavelet basis. For Haar, Daubechies Symlets and Shannon wavelets, Figure 7(a) shows that hierarchic normalized auto-correlation relaxation times do not increase with the dimension d , what verifies that they do not suffer from the phase-transition critical slowing down. It reproduces the absence of critical slowing down observed in [MOBM22] with an Metropolis-Hasting sampling, as we know that the MCMC mixing time tends to an undajusted Langevin diffusion in the continuum time limit [ABBL06, GGR97].

These experiments give a strong indication that log-Sobolev constants of wavelet conditional probabilities are uniformly bounded independently of d , despite the fact that the energy Hessians have negative eigenvalues. This is a mathematical conjecture which has not been proved. Calculations of the log-Sobolev constant of φ^4 have been carried for temperatures above the critical temperature [BD22, BBD23, CE22, BB19], but have not been extended up to the phase transition. As expected, Figure 7(a) also shows that hierarchic normalized auto-correlation relaxation time becomes smaller when improving the frequency localization of wavelets. Shannon wavelets have more vanishing moments and are more regular than Daubechies Symlets which are themselves better localised in frequency than Haar wavelets. Because the Haar wavelet has a poor frequency localization, the coarse graining does not eliminate all the high frequency from φ_{j-1} , which are responsible for big eigenvalues in $\nabla_{\bar{\varphi}_j}^2 \bar{U}_j$. This tail, observed Figure 5(b) requires reducing the time sampling step of the Langevin dynamic, and it increases the normalized relaxation times.

Energy estimation error Approximating scalar potential energies requires to accurately approximate the kinetic energy term and the scalar potential. The Hessian of the kinetic energy is a Laplacian, which is diagonal in a Fourier basis with positive eigenvalues. The scalar potential is non-convex with a Hessian which is diagonal in a Dirac basis with negative eigenvalues. It is the difficult term to estimate.

Hierarchical models can be sampled without estimating the free energies of conditional probabilities. To evaluate the model precision without estimating the free energies, we quantify estimation errors by computing model errors on a sufficient set of moments. These moments are estimated by Monte Carlo, over the data basis of samples of φ^4 and by generating samples with the hierarchic sampling algorithm for each hierarchic model. For scalar potential energies, the sufficient statistics are defined by second order moments and by the marginal distribution of the $\varphi(n)$. Appendix D computes in (84) a Kullback divergence error $e(p, p_\theta)$ which adds a Kullback divergence error from second order moments and from marginal distributions.

Figure 7(b) gives the value of the moment error for hierarchical models computed with Haar, Symlet-4 and Shannon wavelets. These models are learned with large enough data sets so that the variance of statistical estimators becomes negligible. The error is minimum for Haar wavelets. It is much larger for a Symlets-4 wavelet, whose support is 7 times larger. For a Shannon wavelet, which has a slow spatial decay, the estimation error of marginal densities becomes

extremely large. This error comes from the mixing produced by wavelets of wide support. The central limit theorem proves that a linear combination of a sufficiently large number of independent variables converges to a Gaussian. Non-convexities thus disappear from the marginals of wavelet coefficients if their support is too large, but its trace is present in high order interactions of these wavelet variables. This is much more difficult to estimate. This is also why it would be difficult to estimate a φ^4 model in a Fourier basis. The marginal distribution of each Fourier basis is convex, which looks good and simple, but the model estimation then requires incorporating the high order dependencies of Fourier coefficients, to recover the non-convexity of the scalar potential.

Wavelet bases seem to have a near-optimal trade-off to estimate the probability distribution of φ^4 at the phase transition while avoiding the critical slowing down. Surprisingly, the Haar wavelet corresponding to Kadanoff renormalizing group is the best wavelet choice. It minimizes the model estimation error while avoiding the critical slowing down.

5 Robust Multiscale High Order Interactions

Non-Gaussian random fields can have long range interactions across space and scales. In images, it often appears through the existence of sharp transitions which propagate along piece-wise regular curves such as filaments or edges. Non-Gaussian properties may be captured by higher order polynomials, but it typically leads to high-dimensional models and high variance estimators. Section 5.1 introduces low dimensional models of multiscale probability interactions. It defines robust approximations of high order models. Section 5.2 studies numerical applications to modelling and generation of dark matter densities and 2D turbulent vorticities.

5.1 Interactions over Multiple Hierarchies by Wavelet Scattering

Hierarchic models decompose p into a cascade of conditional probabilities across scales, which are rewritten as the conditional probabilities of wavelet coefficients. In the following, we build models of such conditional probabilities, by computing a complex wavelet transform which explicitly provides a complex phase. Non-Gaussian properties are captured with a second wavelet transform, on the complex modulus of the first wavelet transform, leading to low-dimensional models of long-range spatial dependencies and dependencies across scales.

Complex wavelet transform To model the probability distribution of φ_{j-1} conditioned on φ_j , we compute a complex wavelet transform of φ_{j-1} . The complex wavelet coefficients calculated from φ_{j-1} can also be written as convolutions of φ with complex wavelets $\tilde{\psi}_{j',k}$ at scales $2^{j'} \geq 2^j$. They have Q orientations indexed by k , sampled on the grid of φ_{j-1} at intervals 2^{j-1}

$$\left(\varphi * \tilde{\psi}_{j',k}(2^{j-1}n) \right)_n.$$

Let g be the low-pass filter of the coarse-graining operator G which computes φ_{j-1} from φ . Appendix A shows that $\varphi * \tilde{\psi}_{j',k}$ is calculated from φ_{j-1} with an a-trous algorithm. It is a cascade of $j' - j - 1$ convolutions of g , followed by convolutions with a family of complex band-pass filter $\tilde{g} = (\tilde{g}_k)_{k \leq Q}$. These filters are dilated by introducing zeros in between their coefficients. In numerical applications, \tilde{g} has $Q = 4$ Morlet filters specified in Appendix A. At each scale 2^j , they define 4 wavelets $\tilde{\psi}_{j,k}$ whose support is proportional to 2^j . They are approximately rotated by $0, \pi/4, \pi/2$ and $3\pi/4$. Figure 8 show the real and imaginary parts of the wavelets $\psi_{j,k}$ for $j = 3$ computed with these Morlet filters and the Symlet-4 filters g . These complex wavelets have a Hermitian symmetry $\tilde{\psi}_{j,k}(-n) = \tilde{\psi}_{j,k}^*(n)$. Their real and imaginary parts are therefore symmetric and antisymmetric. The lowest frequencies are retained by the scaling filter ϕ_J , that we write $\phi_J = \tilde{\psi}_{J+1,k}$ to simplify notations.



Figure 8: Complex wavelet $\tilde{\psi}_{j,k}$ computed with a 2D Symlet-4 low-pass filter g , and 4 oriented Morlet filters $(\tilde{g}_k)_{k \leq 4}$, at the scale $2^j = 8$. The upper and lower rows show respectively the real part and the imaginary parts of $\tilde{\psi}_{j,k}$, for $k = 1, 2, 3, 4$.

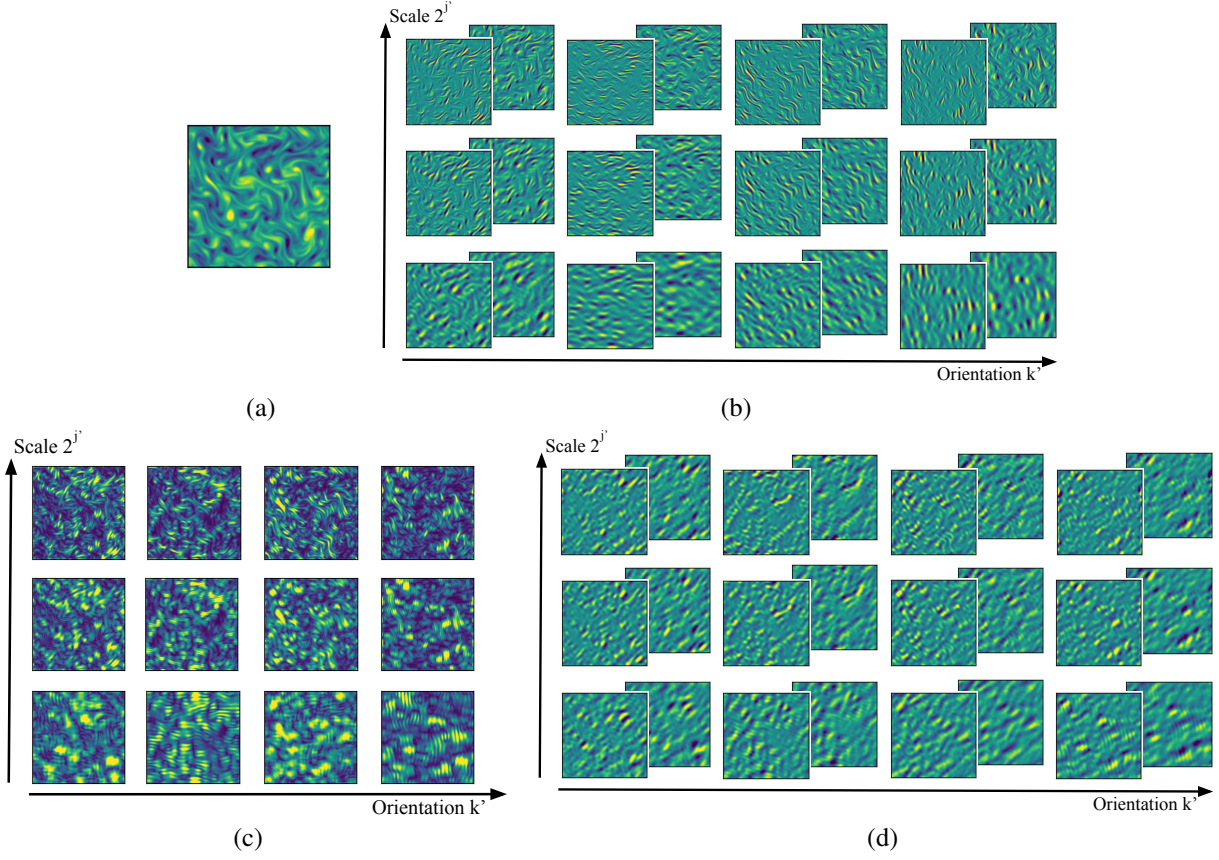


Figure 9: (a): φ_{j-1} is a vorticity field of a 2D turbulence. (b): Complex wavelet transform at scales $2^{j'} \geq 2^j$ computed from φ_{j-1} without subsampling. Foreground and background images show respectively the real and imaginary parts of $\varphi * \tilde{\psi}_{j',k'}$, computed with Morlet type wavelets. Each row corresponds to a scale $2^{j'} \geq 2^j$ and each column to the $Q = 4$ orientation indices k' . (c) Modulus $|\varphi * \tilde{\psi}_{j',k'}|$ of wavelet coefficient images. They have a large amplitude at sharp transitions, with long-range dependencies in space and across scales and orientations. (d) The foreground and background images are the real and imaginary parts of $|\varphi * \tilde{\psi}_{j',k'}| * \tilde{\psi}_{\ell,k}$ for different j' and k' , and for a fixed $\ell = 3$ and $k = 1$. These images look alike, which shows that wavelet coefficient modulus $|\varphi * \tilde{\psi}_{j',k'}|$ have strong dependencies across scales $2^{j'}$ and orientations k' .

Figure 9(b) shows the wavelet coefficients of a vorticity image of 2D turbulence field. The wavelet coefficients of such a stationary field are almost not correlated across scales, because wavelets have a Fourier transform localized in different frequency bands. Wavelet coefficients in different frequency bands have phases which oscillate at different rates or along different orientations, which cancel correlations. However, the amplitudes $|\varphi * \tilde{\psi}_{j',k}|$ of wavelet coefficients are strongly correlated across scales, as shown by Figure 9(b). The vorticity field has sharp variations which create large amplitude wavelet coefficients at the same positions over multiple scales and orientations.

Wavelet scattering Most wavelet modulus $|\varphi * \tilde{\psi}_{j',k'}|$ have long range spatial dependencies. This long range dependency is represented by local interactions with a second hierarchic decomposition, computed with a second wavelet transform of $|\varphi * \tilde{\psi}_{j',k'}|$.

The wavelet coefficients $\varphi * \psi_{j',k'}$ and the second wavelet transform of $|\varphi * \psi_{j',k'}|^q$ for $q = 1$ or $q = 2$ are incorporated into a vector of scattering coefficients:

$$S_{j'}(\varphi_{j-1}) = \left(\begin{array}{c} \varphi * \tilde{\psi}_{j',k'}(2^{j-1}n) \\ |\varphi * \tilde{\psi}_{j',k'}|^q * \tilde{\psi}_{\ell,k}(2^{j-1}n) \end{array} \right)_{\ell \geq j', k, k' \leq Q, n}. \quad (54)$$

If $q = 2$ then upper and lower terms of $S_{j'}$ are polynomials of degree 1 and 2 of the values $\varphi(n)$. If $q = 1$ then each term remains Lipschitz, but the complex modulus may create singularities when complex wavelet coefficients vanish, which is addressed by replacing $|z|$ by $(|z|^2 + \epsilon)^{1/2}$, for a small ϵ . Scattering coefficients $|\varphi * \tilde{\psi}_{j',k'}|^q * \tilde{\psi}_{\ell,k}$ are indexed by two scales $2^{j'} \geq 2^j$ and $2^\ell \geq 2^{j'}$. This double hierarchy measures the variations of $|\varphi * \tilde{\psi}_{j',k'}|^q$ over neighborhoods of sizes proportional to 2^ℓ , in a direction indexed by k . Figure 9(b) shows these scattering coefficients for a fixed (ℓ, k) .

Robust scattering interaction energies We introduce a hierarchic probability model from scattering coefficients. At the largest scale 2^J , the Gibbs energy model $U_{\theta_J} = \theta_J^T \Phi_J$ of $p_{\theta_J}(\varphi_J)$ is defined with a quadratic term and a scalar potential, as in (47). At scales $2^j \geq 2^J$, we define a Gibbs energy model $\bar{U}_{\bar{\theta}_j}$ of $p(\bar{\varphi}_j|\varphi_j)$ from interactions of scattering coefficients. Let z^T be the complex conjugate transpose of the complex valued vector z . The energy model includes two point interactions between scattering coefficients S_j at the scale 2^j with $S_{j'}$ for $2^{j'} \geq 2^j$, plus a scalar potential:

$$\bar{U}_{\bar{\theta}_j} = \sum_{j'=j}^{J+1} S_j^T K_{j,j'} S_{j'} + \bar{V}_{\bar{\gamma}_j} = \bar{\theta}_j^T \Psi_j, \quad (55)$$

where

$$\Psi_j = \begin{pmatrix} S_j S_j^T \\ \Gamma \end{pmatrix}_{j' \geq j} \quad \text{and} \quad \bar{\theta}_j = \begin{pmatrix} K_{j,j'} \\ \bar{\gamma}_j \end{pmatrix}_{j' \geq j}. \quad (56)$$

The dimensionality of this model can be reduced from known symmetries of p . If p is stationary, then $p_{j-1}(\varphi_{j-1})$ is invariant to translation. The translation invariance of $\bar{U}_{\bar{\theta}_j}$ is equivalent to imposing that each $K_{j,j'}$ is a convolutional operator over the spatial grid of φ_{j-1} . Symmetries to actions of other groups can be enforced with other conditions discussed in the next section.

If $q = 2$, then the coordinates of each $S_{j'}$ are polynomials of degree 1 and 2 of the values $\varphi_{j-1}(n)$, so each interaction term $S_j^T K_{j,j'} S_{j'}$ is a polynomial of degree 4. If $q = 1$, then the complex wavelet phase is treated similarly but $\bar{U}_{\bar{\theta}_j}$ has a quadratic growth in φ as opposed to a degree 4. It is obtained by replacing $|z|^2$ by $|z|$. The polynomial of degree 4 is changed into a polynomial of degree 2 with phase harmonics, whose properties are studied in [ZM21]. It improves statistical robustness because $|z|$ is Lipschitz as opposed to $|z|^2$. Similarly to a linear rectifier used in neural networks, $|z|$ is homogeneous and can be computed as a linear combination of rectifiers [ZM21]. Models computed with $q = 1$ have similar properties to models computed with $q = 2$, but are often more accurate because of their statistical robustness studied in the next section.

Local scattering spectrum interactions A hierarchic organization aims at creating the needed long-range interactions through local interactions in the hierarchy. Similarly, a scattering spectrum defines long-range models of stationary fields with local low-dimensional interactions among scattering coefficients.

A scattering spectrum interaction model is constructed by eliminating the interaction terms in (55) which are a priori negligible. For stationary probabilities, the interaction matrices $K_{j,j'}$ are convolution operators. Images of $S_{j'}$ are complex wavelet coefficient computed with $\tilde{\psi}_{j',k'}$ or with $\tilde{\psi}_{\ell,k}$ for $2^\ell \geq 2^{j'}$. Two images of S_j and $S_{j'}$ have an energy mostly concentrated in disjoint frequency domains if they are computed with different wavelets. Their interaction thus has a negligible contribution to the energy $\bar{U}_{\bar{\theta}_j}$ because each $K_{j,j'}$ in (55) is convolutional.

Two images of S_j and $S_{j'}$ computed with a same $\tilde{\psi}_{\ell,k}$ have a priori a non-zero interaction. A scattering spectrum model further assumes that wavelet coefficient interactions are local in space. This assumption is valid for multiscale stationary processes which do not produce oscillatory phenomena. A scattering spectrum model keeps only the interaction of pairs of scattering coefficients in S_j and $S_{j'}$ which have the same spatial position.

The resulting scattering spectrum model assumes that interactions are local in space and over the scattering scales. However, it defines long-range interactions in space and across the wavelet coefficients of the original image φ . Appendix B shows that this scattering spectrum model reduces Ψ_j to a vector of dimension $O(\log^2 d)$ if φ has a dimension d . The full hierarchic energy model U_θ aggregates the interaction models $\bar{U}_{\bar{\theta}_j}$ at all scales $d \geq 2^j \geq 1$. It is thus defined by a coupling vector θ of dimension $O(\log^3 d)$.

Stationary Scattering Energy Model We give an analytical formulation of the stationary scattering energy model U_θ obtained from interaction energy models $\bar{U}_{\bar{\theta}_j}$ at all scales 2^j . It is calculated with hierarchic stationary potentials defined from the scattering interaction energies Ψ_j in (55). Let us write the complex wavelet transform of φ

$$W\varphi = \left(\varphi * \tilde{\psi}_{j,k}(n) \right)_{0 < j \leq J+1, k, n}, \quad (57)$$

This wavelet transform without subsampling is computed with the a-trous algorithm of Appendix A. From $\varphi_j = \varphi * \phi_j(2^j n)$, Appendix A shows that the a-trous algorithm computes wavelet coefficients of φ at scales $2^J \geq 2^{j'} \geq 2^j$ subsampled at intervals 2^j . We write

$$R(\varphi_j) = \left(\begin{array}{c} \varphi * \phi_j(2^j n) \\ |\varphi * \tilde{\psi}_{j',k'}(2^j n)|^q \end{array} \right)_{j' \geq j, k', n}.$$

If $f = (f_k)_k$ is a family of real valued fields, we also write $f * f^\top = (f_k * f_{k'}^\top)_{k,k'}$ with $f_k^\top(n) = f_k(-n)$.

Theorem 5.1. *The potentials*

$$\Phi_j(\varphi_j) = \left(\begin{array}{c} R(\varphi_j) * R(\varphi_j)^\top \\ \Gamma(\varphi_j * \phi_\ell) \end{array} \right)_{J-j \geq \ell \geq 0} \quad (58)$$

are stationary hierarchic with interactions Ψ_j defined in (55). Regressing each free energy F_j over Φ_j defines a fine scale Gibbs stationary model

$$U_\theta(\varphi) = \frac{1}{2} \varphi^\top K \varphi + \sum_{j=0}^J V_j(\varphi) + V_{\text{int}}(\varphi), \quad (59)$$

with $V_j(\varphi) = \gamma_j^\top \Gamma(\varphi * \phi_j)$ and

$$V_{\text{int}}(\varphi) = \varphi^\top L (|W\varphi|^q) + \frac{1}{2} (|W\varphi|^q)^\top M (|W\varphi|^q), \quad (60)$$

where γ_j and the convolution operators (K, L, M) are computed with a linear coupling flow equation.

The proof is in Appendix E.4. When $q = 2$, the interaction potential is thus a sum of third order and fourth order polynomials which capture interactions between wavelet coefficients at the scale 2^j and larger scales. Setting $q = 1$ gives a robust approximation, where all terms have a quadratic growth. The convolutional matrices L and M have non-local kernels in space. A local scattering spectrum model only keeps interaction coefficients between pairs of scattering coefficients computed with a same wavelet, at a same position. It implies that $K = W^\top K' W$, $L = W^\top L' W$ and $M = W^\top M' W$, where K' is diagonal and L' and M' are block diagonal convolutional matrix, with a total of $O(\log^3 d)$ non-zero interaction coefficients.

5.2 Numerical Applications to Dark Matter and Turbulence Fields

We evaluate the precision of hierarchical wavelet scattering models U_θ for two types of non-Gaussian physical fields having coherent geometric structures. We compute the Langevin normalized auto-correlation relaxation time as a proxy to evaluate the evolution of normalized log-Sobolev constants, after renormalization.

Numerical experiments are carried on 2D fields of dark matter images, which are the logarithm of 2D slices of simulated 3D large-scale distribution of dark matter in the Universe [VNHM⁺20] shown in Figure 10(a). We also model 2D turbulence vorticity fields of incompressible 2D fluids stirred at the scale around 32 pixels, at a fixed time, simulated from 2D Navier-Stokes equations [SZFA06], shown in Figure 10(a). The time evolution of 2D turbulence is an inverse cascade which transfers the energy towards the lowest scales [Kra67]. The 2D Navier-Stoke simulation initialized with a Gaussian white noise at $t = 0$ defines a transport of this Gaussian white distribution into a stationary distribution at a fixed t . The vorticity field is stationary in space at a fixed time, but it does come from a system at equilibrium in time. There is no closed formula for Hamiltonians of such out of equilibrium systems, except in particular 1D cases [DLS02, BDSG⁺15]. Both datasets (100 and 3000 independent realizations) have periodic boundary conditions and are down-sampled to $d = 128^2$ pixels. They are augmented with rotations and spatial symmetries because their probability distribution is isotropic.

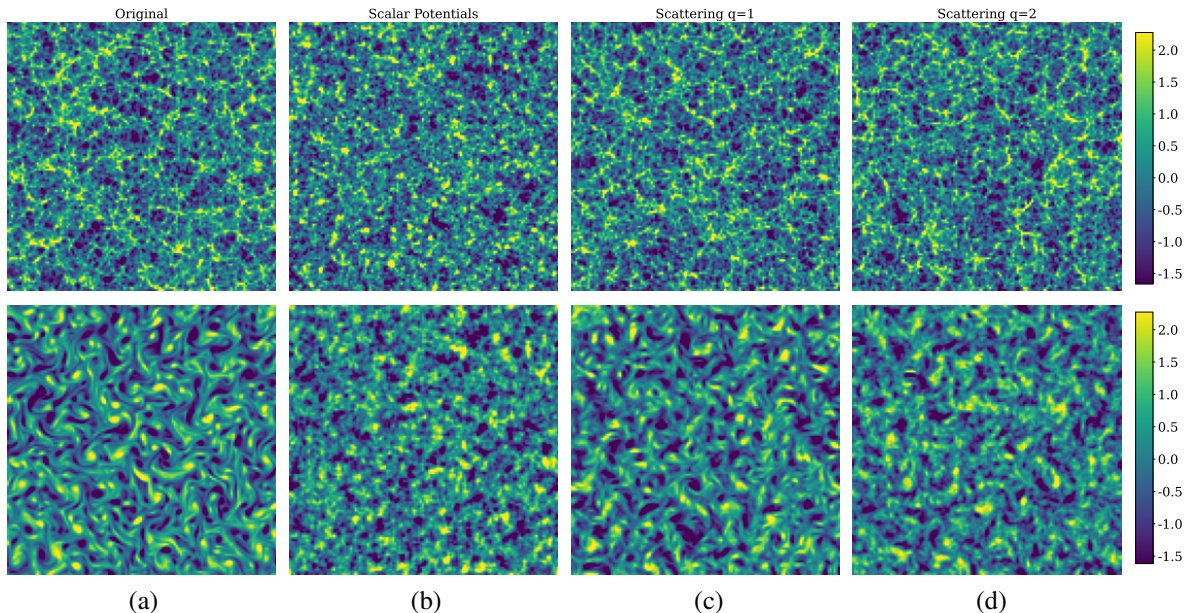


Figure 10: (a): Top row: 2D slide of a 3D dark-matters density simulation [VNHM⁺20]. Bottom row: vorticity fields of a 2D periodic turbulent flow at a fixed time t , generated numerically with the 2D Navier Stokes equation from an initial Gaussian white noise [SZFA06]. (b): Samples of the hierarchical scalar potential model defined in (49). (c): Samples of the hierarchic wavelet scattering model, with an exponent $q = 1$. (d): Same as (c) with an exponent $q = 2$.

Hierarchic model generations Figure 10 (b,c,d) shows images generated from hierarchical models, respectively with a scalar potential, robust wavelet scattering interactions with $q = 1$ and higher order wavelet scattering with $q = 2$. Over all scales, the scalar potential model and the wavelet scattering models have respectively about 300 and 2500 coupling parameters. There is no scalar potential term in the scattering models.

Generations from scalar potential models in Figure 10(b) do not restore random geometric structures appearing in the original fields. For dark matter fields, the wavelet scattering models in Figure 10(c,d) reproduce well the visual texture of these images. For the vorticity fields of 2D turbulence, eddies and vorticity flows are well reproduced only with $q = 1$ but are degraded for $q = 2$. Indeed, as shown by (12) and in Appendix C.1, computing the coupling flow parameters θ_j of the hierarchical model requires inverting a matrix of empirical moments estimated on the training dataset. Higher order polynomials amplify outliers. It increases the estimation variance of high order moments, and thus introduces more errors. As expected, the scattering model with $q = 1$ is more robust than the high order model with $q = 2$. For turbulence images, estimation errors can introduce a divergence of the Langevin diffusion at the finest scale, where the spectrum has a fast decay. This is avoided by adding a small confinement term for large amplitude coefficients. It adds $\epsilon D_j \bar{\varphi}_j^A$ to the energy $\bar{U}_{\bar{\theta}_j}$. The value of ϵ is about 10 times larger for $q = 2$ than for $q = 1$, which affects the generated image quality.

Langevin relaxation time The renormalization aims at reducing the amplitude of normalized log-Sobolev constant to estimate a model by score diffusion with as few samples as possible and to reduce the computational complexity of the Langevin diffusion. A necessary condition is to control the largest eigenvalue of the covariance and its condition number. As explained in Section 3.6, a hierarchical model must use wavelets having enough vanishing moments and which are sufficiently regular. For Dark matter images and turbulence fields, we respectively use Symlet-3 and Symlet-4 wavelets. These dark matter and 2D turbulence images have a power spectrum which decays faster than a power law at the highest frequencies. To renormalize the smallest eigenvalues of the covariance at high frequencies, Section 3.6 also explains that $\bar{\varphi}_j$ can be represented in a wavelet packet basis having a sufficient frequency resolution. The wavelet packet filtering (22) reduces the width of wavelet frequency supports by a factor 2^{a_j} . In numerical experiments, we set $a_j = \min(a, J - j)$ and we adjust a . For $a = 0$, the wavelet-packet basis is a wavelet basis. Choosing a wavelet packet basis as opposed to a wavelet basis does not modify the hierarchic energy model. It only modifies the coordinate system representing $\bar{\varphi}_j$ and hence the renormalization which modifies the log-Sobolev constant.

Figure 11 gives the evolution of the Langevin normalized auto-correlation relaxation time τ of the hierarchical model in (53), as a function of the system size d . For $a = 0$ corresponding to wavelets, the relaxation time τ increases with

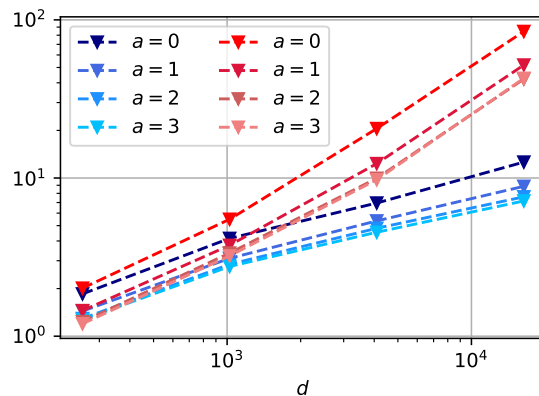


Figure 11: Langevin normalized auto-correlation relaxation time (53) for scattering hierarchical models computed in wavelet or wavelet packet bases, with $a_j = \min(a, J - j)$, as a function of the image size d . Langevin relaxation time for dark matter, (computed with $q = 2$, in a Symlet-3 basis) are in blue and for dark-matter fields (computed with $q = 1$, in a Symlet-4 basis) in red. Increasing the wavelet packet Fourier resolution with a slightly reduces the relaxation time, but it does not avoid an exponential growth with d .

the system size d , both for dark-matter and turbulence fields. This is different from the relaxation time of hierarchical models of φ^4 shown in Figure 7(a), which does not grow with d . However, after renormalization, the relaxation time for dark-matter and turbulence is 3 orders of magnitude below the one for φ^4 without any renormalization. It shows that the hierarchical renormalization accelerates considerably the sampling, although it still degrades with d .

Increasing the frequency resolution of wavelet packets with a has a small effect on the Langevin relaxation time growth in Figure 11. The remaining growth is due to the non-Gaussian multiscale behavior of the model. It is produced by scaling properties of third and fourth order energy components, which are different from second order scaling properties of the covariance, and are therefore not compensated by a renormalization based on the covariance. Such phenomena appear in multifractal random processes [Jaf04, AGV13]. The scattering model generated in Figure 10 (b,c) are calculated by renormalizing wavelet coefficients in a wavelet packet basis, with $a = 3$ for turbulence images and with $a = 2$ for dark matter fields.

Hierarchical model precision We have no energy model for the dark matter and turbulence fields used in numerical experiments. The model precision is thus evaluated numerically over a family of standard moments used in statistics and physics. We test the distribution of point-wise marginals, the Fourier spectrum (second order moments), the bi-spectrum (third order moments) also calculated in the frequency domain, and structure functions. Each moment is estimated with a Monte Carlo sum over m training samples of p . These moments are compared with moments of hierarchical models, also estimated with a Monte Carlo sum over enough model samples generated by MALA sampling.

Figure 12(a,b) show that scalar potential models generate stationary fields φ , where $\varphi(n)$ have a marginal distribution nearly equal to the marginals of the original fields, since the model is optimized from these marginals. The same result is obtained for the wavelet scattering models, although they do not incorporate a scalar potential which imposes these marginal moments. All models reproduce well the power spectrum, which is only specified in these models by a reduced diagonal matrix with less than $\log d$ wavelet second order moments.

The bi-spectrum is a third-order moments computed over Fourier coefficients, which is zero for a Gaussian process. It is also zero if $p(\varphi) = p(-\varphi)$ which is the case for the 2D turbulence vorticity. It is thus only computed for the dark-matter density images. The bi-spectrum calculation is explained in Appendix F.2. Figure 12(d) shows that the bi-spectrum is well reproduced by a wavelet scattering model with $q = 2$, which incorporates third order polynomial terms. It is also well reproduced with $q = 1$. This robust model does not include third order terms but a lower order equivalent term which is also antisymmetric. On the opposite, the bi-spectrum of the scalar potential model is quite different from the bi-spectrum of the original dark-matter field.

Kolmogorov structure functions[kol41] are moments of order m over the field of increments, indexed by the spatial lag δ

$$\text{SF}_m(\delta) = \mathbb{E}_p(|\varphi(n) - \varphi(n - \delta)|^m). \quad (61)$$

Figures 12(e,f) plot the structure functions respectively for $m = 1$ and $m = 4$ since $2nd$ and $3rd$ order moments have already been evaluated. The only model providing an accurate approximation both for the turbulence and dark-matter

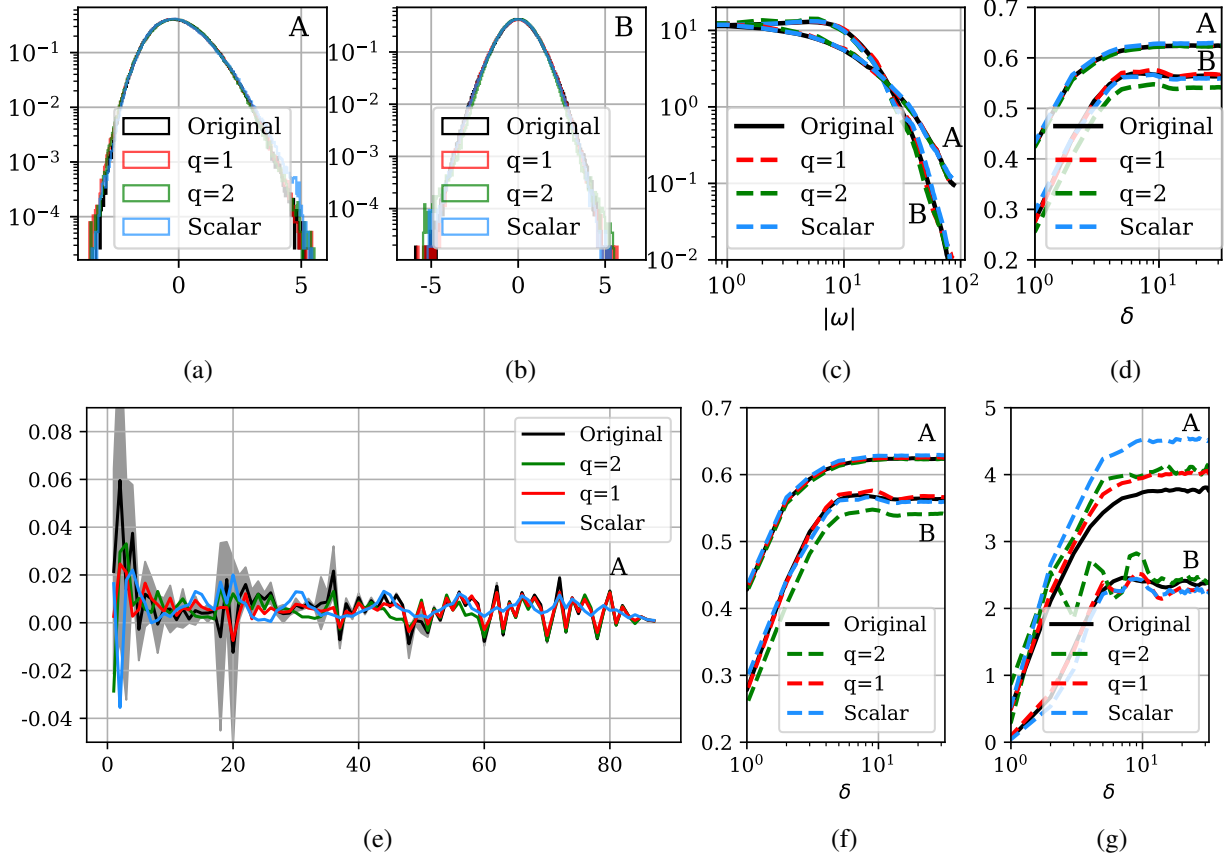


Figure 12: Each graph shows a specific family of moments estimated on the training data (in black) and on samples of a hierarchical model (wavelet scattering with $q = 1$ in red, with $q = 2$ in green, and scalar potential model in blue). Models are labeled (A) for dark-matter and (B) for 2D turbulence. Gray zones represent the estimation variance of these higher order moments over the training dataset. (a,b): marginal probability densities of $\varphi(n)$. (c): covariance eigenvalues (power-spectrum). (d): Structure function of order $m = 1$ as a function of δ . (e): third order bi-spectrum moments, ordered from low to high frequencies. Not shown for the 2D turbulence (B), because they all vanish. (f): Structure function of order $m = 4$. (g): Structure function of order $m = 6$.

fields is the robust wavelet scattering model for $q = 1$. The error of the wavelet high-order model for $q = 2$ over the turbulence field is due to the larger regularization needed to confine the Langevin diffusion. The reproduction of higher order moments slowly degrade when increasing the order of the moments. Figure 12(g) shows that none of the model faithfully reproduces the structure function of order 6 on dark matter, but it is well reproduced on the turbulence which is more Gaussian.

Two-point interaction model Since the wavelet scattering model have no scalar potential, Theorem 5.1 proves that the stationary model is characterized by 3 convolutional operators: K, L, M in (59). They are computed from the learned interaction parameters $\bar{\theta}_j$ at each scale, with the coupling flow equation (41). Figure 13(a,b) shows the convolution kernel K for turbulence and dark-matter datasets. Both kernels are local in space and nearly isotropic, which is not imposed by the model. They resemble to a Laplacian. Figure 13(c) shows their Fourier transform as a function of the frequency amplitude $|\omega|$. The estimated kernel for 2D turbulence has higher eigenvalues at high frequencies than the one for dark matter, what is coherent with the faster decrease of its power spectrum.

6 Conclusion

Hierarchic models provide an inverse renormalization group decomposition of probability distributions into conditional probabilities in wavelet bases. The renormalization partly avoids the bad conditioning of learning and sampling algorithms, by reducing log-Sobolev constants. For the φ^4 model, we conjecture that it eliminates the critical slowing down, as shown by numerical experiments.

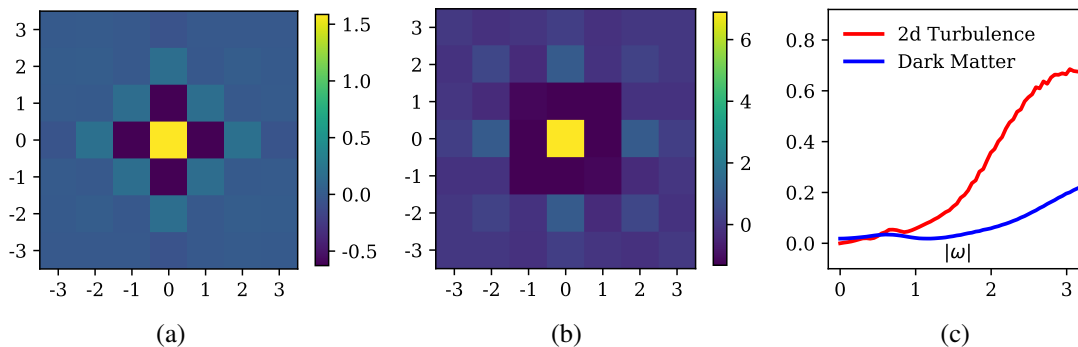


Figure 13: Estimated 2-point convolutional kernel K of U_θ defined in eq. (59), for $q = 1$. (a): kernel for dark matter images. (b): kernel for 2D turbulence. They are local and nearly rotation invariant. (c): Fourier transform of each kernel as a function of $|\omega|$.

For multiscale non-Gaussian processes such as dark matter distribution or 2D turbulence, we introduced a low-dimensional wavelet scattering model, based on robust multiscale high order interactions. Numerical tests show that they can provide an accurate model of complex fields beyond scalar potential models, but we remain far from a satisfying model of turbulence. More complex structures appear in 3D where the energy cascade is not inverted, and we do not consider the time evolution.

Numerical experiments show that robust multiscale scattering models improve the estimation by reducing the amplitude growth of high order polynomials. As opposed to φ^4 , for turbulence and dark-matter fields, the renormalization reduces but does not avoid the exponential increase of log-Sobolev constants with the field dimension. Moreover, estimation errors can create a divergence of Langevin diffusions, if not regularized.

Regularization issues can be addressed by replacing the Langevin diffusion by a score diffusion [SSK⁺21, RBL⁺22] for each $\bar{p}_{\bar{\theta}_j}(\bar{\varphi}_j|\varphi_j)$, as in [GCDBM22]. An integrated renormalization group approach of score diffusion and multiscale coarse graining schemes is proposed in [CR23]. This is also motivated by the spectacular results of score diffusion generations with deep neural networks, and particularly with U-Nets [RFB15] which integrate multiscale image decompositions. Understanding the correspondence between these multiscale deep network decompositions and robust high order wavelet scattering energies is yet another challenging question.

Acknowledgments

This work was supported by a grant from the PRAIRIE 3IA Institute of the French ANR-19-P3IA-0001 program. We thank Rudy Morel, Erwan Allys and Misaki Ozawa for providing the training datasets. We also thank Nathanaël Cuvellé-Magar and Jean-Baptiste Himbert for feedback on the manuscript.

A Wavelet Transforms

We review the properties of real and complex wavelet transforms computed by iterating over low-pass and band-pass filters, in one and two dimensions.

Conjugate mirror filters Orthogonal wavelets are computed with conjugate mirror filters. In dimension $r = 1$, a pair of conjugate mirror filter (g, \bar{g}) includes a low-pass filter g whose Fourier transform $\hat{g}(\omega) = \sum_n g(n)e^{-in\omega}$ satisfies

$$|\hat{g}(\omega)|^2 + |\hat{g}(\omega + \pi)|^2 = 2 \text{ and } \hat{g}(0) = \sqrt{2}. \quad (62)$$

The second filter \bar{g} has a single high-pass filter defined by $\bar{g}(n) = (-1)^{1-n} g(1-n)$. One can verify that the resulting convolution and subsampling operators

$$G\varphi(n) = \varphi * g(2n) \text{ and } \bar{G}\varphi(n) = \varphi * \bar{g}(2n) \quad (63)$$

define an orthogonal matrix $\begin{pmatrix} G \\ \bar{G} \end{pmatrix}$ [Mal09]. All convolutions are computed with periodic boundary conditions.

For images ($r = 2$), two-dimensional conjugate mirror filters are computed as separable products of one-dimensional conjugate mirror filters (g, \bar{g}) [Mal09]. For $n = (n_1, n_2)$ there is a single two-dimensional separable low-pass filter $g(n_1, n_2) = g(n_1)g(n_2)$ and 3 high-pass filters in $\bar{g} = (\bar{g}_k)_{1 \leq k \leq 3}$, with

$$\bar{g}_1(n_1, n_2) = g(n_1)\bar{g}(n_2), \bar{g}_2(n_1, n_2) = \bar{g}(n_1)g(n_2), \bar{g}_3(n_1, n_2) = \bar{g}(n_1)\bar{g}(n_2).$$

The convolutional operator G and \bar{G} in two dimensions are still defined by (63) with these two-dimensional separable filters, and $\bar{G}\varphi$ has 3 output images.

A-trous filters Averaged coefficients and wavelet coefficients are iteratively computed for $j > 0$ with

$$\varphi_j(n) = \varphi_{j-1} * g(2n) \quad \text{and} \quad \bar{\varphi}_j = \varphi_{j-1} * \bar{g}(2n). \quad (64)$$

These coefficients can be written as convolutions of the input $\varphi = \varphi_0$ with a scaling filter ϕ_j and wavelets $\psi_{j,k}$ subsampled by 2^j :

$$\phi_j = (\varphi * \phi_j(2^j n))_n \quad \text{and} \quad \bar{\varphi}_j = (\varphi * \psi_{j,k}(2^j n))_{k,n}. \quad (65)$$

These scaling filters and wavelets satisfy recursive equations computed with "a-trous" filters resulting from the cascaded subsampling. In one dimension, for any filter h we write h_j the a-trous filter such that $h_j(2^j n) = h(n)$ and $h_j(n) = 0$ if $2^{-j}n$ is not an integer in one dimension or does not belong to the two-dimensional grid \mathbb{N}^2 in two dimensions. The a-trous filter h_j is a dilation of h by 2^j , by setting intermediate coefficients to zero. One can derive from (64) that

$$\phi_j = \phi_{j-1} * g_{j-1} \quad \text{and} \quad \psi_{j,k} = \phi_{j-1} * \bar{g}_{j-1,k}. \quad (66)$$

Scaling filters and wavelets are thus obtained with a cascade of a-trous filters. One can verify that

$$\varphi_j * \phi_\ell(n) = \varphi_{j-1} * \phi_{\ell+1}(2n), \quad (67)$$

and

$$\varphi_j * \psi_\ell(n) = \varphi_{j-1} * \psi_{\ell+1}(2n). \quad (68)$$

Asymptotic wavelet bases When j goes to ∞ , for appropriate filters \bar{g} and low-pass filters g , one can prove [Dau92] that ϕ_j and $\psi_{j,k}$ converge to $\phi(x)$ and wavelets $\psi_k(x)$, up to a dilation by 2^j . These limit functions are square integrable, $\int |\phi(x)|^2 dx < \infty$ and $\int |\psi_k(x)|^2 dx < \infty$. In 1 dimension, conjugate mirror filters define a scaling function $\phi(x)$ and a single asymptotic wavelet $\psi(x)$ whose Fourier transforms $\hat{\phi}(\omega)$ and $\hat{\psi}(\omega)$ satisfy

$$\hat{\psi}(\omega) = \frac{1}{\sqrt{2}} \hat{g}(2^{-1}\omega) \hat{\phi}(2^{-1}\omega) \quad \text{with} \quad \hat{\phi}(\omega) = \prod_{q=1}^{+\infty} \frac{\hat{g}(2^{-q}\omega)}{\sqrt{2}}.$$

If we impose that $\hat{g}(\omega) > 0$ for $\omega \in [-\pi/2, \pi/2]$, then one can prove [Mal09] that $\{2^{-j/2}\psi(2^{-j}x - n)\}_{n \in \mathbb{Z}, j \in \mathbb{Z}}$ is an orthonormal basis of $\mathbf{L}^2(\mathbb{R})$. If we limit the maximum scale to 1, with periodic boundary conditions, we obtain an orthonormal basis of $\mathbf{L}^2([0, 1]^2)$. Wavelets with non-periodic boundary conditions may also be designed [Dau92].

A Haar filter is the conjugate mirror filter having a minimum size spatial support: $g(n) = 1$ if $n = 0, 1$ and $g(n) = 0$ otherwise. It defines the Haar wavelet ψ shown in Figure 14(a). The Shannon low-pass filter has a Fourier transform having a minimum size support: $\hat{g} = 1_{[-\pi/2, \pi/2]}$. It defines a Shannon wavelet, shown in figure 14(c). A Daubechies Symlet filter g of order m [Dau92] has a support of size $2m - 1$ and defines a compactly supported wavelet having m vanishing moments:

$$\forall 0 \leq k < m, \quad \int x^k \psi(x) dx = 0.$$

These integrals imply that $\hat{\psi}$ and its $m - 1$ first derivatives vanish at the frequency $\omega = 0$ and hence that $|\hat{\psi}(\omega)| = O(|\omega|^m)$. A Symlet filter is as symmetric as possible [Dau92]. The regularity of ψ also increases with m . The Symlet-4 wavelet is shown in figure 14(b).

Complex Morlet filters Complex wavelets $\tilde{\psi}_{j,k}$ are defined by replacing the real filters $\bar{g} = (\bar{g}_k)_k$ by a family of complex filters $\tilde{g} = (\tilde{g}_k)_k$. Similarly to (66)

$$\phi_j = \phi_{j-1} * g_{j-1} \quad \text{and} \quad \tilde{\psi}_{j,k} = \phi_{j-1} * \tilde{g}_{j-1,k}, \quad (69)$$

where $\tilde{g}_{j,k}$ is the a-trous filter defined from \tilde{g}_k .

In numerical applications we use $Q = 4$ complex Morlet filters $\tilde{g} = \{\tilde{g}_k\}_{k \leq Q}$ defined by

$$\tilde{g}_k(n_1, n_2) = \gamma e^{-\eta(n_1^2 + n_2^2)} (e^{i\xi(n_1 \cos \alpha_k + n_2 \sin \alpha_k)} - \beta_k), \quad (70)$$

$\alpha_k = k\pi/Q$ and each β_k is adjusted so that $\sum_{n_1, n_2} \tilde{g}_k(n_1, n_2) = 0$. We choose $\eta = 1.67$ and $\xi = \pi$. Figure 8 shows the two-dimensional complex wavelets $\tilde{\psi}_{j,k}$, computed with the 2D separable low-pass Symlet-4 conjugate mirror filter g and these complex Morlet filters \tilde{g} .

At the very large scales close to the image size, to avoid issues created by periodic boundary conditions, the filters \tilde{g}_k are modified. They are constructed from the analytic part of the conjugate filters $\{\bar{g}_k\}_{k \leq 3}$ associated to g . Computing the analytic part amounts to restrict the Fourier transform over half of the Fourier plane [Mal09], which defines a complex filter. The third diagonal filter is divided into two analytic filters located in the two diagonal directions.

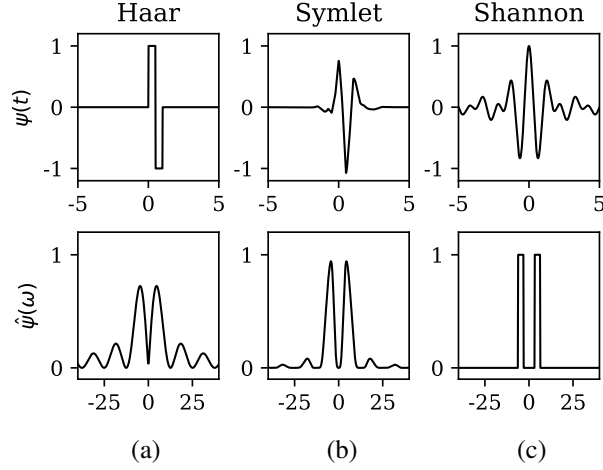


Figure 14: Top row: Graphs of different one-dimensional wavelets $\psi(t)$. Bottom row: Graphs of their Fourier transform modulus $|\hat{\psi}(\omega)|$. (a) Haar (1 vanishing moment), (b) Daubechies Symlet (4 vanishing moments), (c) Shannon Wavelet.

A-trous wavelet transform For any $j > 0$, $\varphi_j(n) = \varphi * \phi_j(2^j n)$. Moreover, (69) implies that, for $j \leq j'$,

$$\tilde{\psi}_{j',k} = \phi_{j-1} * g_{j-1} * \dots * g_{j'-2} * \tilde{g}_{j'-1}.$$

One can thus verify that $\varphi * \tilde{\psi}_{j',k}(2^{j-1}n)$ is calculated from φ_{j-1} by an a-trous algorithm which cascades convolutions with dilated low-pass filters g and the complex Morlet wavelet filter \tilde{g}_k

$$\varphi * \tilde{\psi}_{j',k}(2^{j-1}n) = \varphi_{j-1} * g * \dots * g_{j'-j-1} * \tilde{g}_{j'-j,k}(n). \quad (71)$$

The complex wavelet transform W in (57) is computed by convolutions with ϕ_j and $\tilde{\psi}_j$ without subsampling. Since these filters are cascade of a-trous filters g_j and \tilde{g}_j in (69), these convolutions can be calculated as a cascade of a-trous filterings, from $\varphi = \varphi_0$:

$$\varphi * \tilde{\psi}_{j,k}(n) = \varphi * g * \dots * g_{j-2} * \tilde{g}_{j-1}(n). \quad (72)$$

B Scattering Spectrum Interactions

This appendix specifies scattering spectrum interaction matrices $K_{j,j'}$, for the wavelet scattering model (55), with

$$S_{j'}(\varphi_{j-1}) = (\varphi * \tilde{\psi}_{j',k}(2^{j-1}n), |\varphi * \tilde{\psi}_{j',k'}|^q * \tilde{\psi}_{\ell,k}(2^{j-1}n))_{k,k' \leq Q, \ell \geq j', n}.$$

A scattering spectrum model for stationary processes retains interactions between coefficients of S_j and $S_{j'}$ in (55) computed with the same wavelets at a same spatial position. The pairs of coefficients of S_j and $S_{j'}$ which interact are thus

$$\varphi * \tilde{\psi}_{j,k}(2^{j-1}n) \text{ and } \varphi * \tilde{\psi}_{j',k}(2^{j'-1}n) \text{ for } j' = j, 1 \leq k \leq Q, \quad (73)$$

$$|\varphi * \tilde{\psi}_{j,k'}|^q * \tilde{\psi}_{\ell,k}(2^{j-1}n) \text{ and } \varphi * \tilde{\psi}_{j',k}(2^{j-1}n) \text{ for } j' = \ell, 1 \leq k', k \leq Q, \quad (74)$$

$$|\varphi * \tilde{\psi}_{j,k'}|^q * \tilde{\psi}_{\ell,k}(2^{j-1}n) \text{ and } |\varphi * \tilde{\psi}_{j',k''}|^q * \tilde{\psi}_{\ell,k}(2^{j-1}n) \text{ for } \ell \geq j' \geq j, 1 \leq k, k', k'' \leq Q. \quad (75)$$

For translation invariant energies, the translation invariant version of the potential Ψ_j in (56) has four interaction potentials:

$$\Psi_j = (\Gamma, \Lambda_{2,j}, \Lambda_{3,j}, \Lambda_{4,j}). \quad (76)$$

The potential vector Γ defined in (48) provides an approximation of scalar potentials. For the other 3 potentials, we only keep interactions between coefficients computed with a same wavelet at a same position. The interactions (73) give the average of squared wavelet coefficients in each direction k :

$$\Lambda_{2,j}(\varphi_{j-1}) = \left(\sum_n |\varphi * \tilde{\psi}_{j,k}(2^{j-1}n)|^2 \right)_{k \leq Q}. \quad (77)$$

They provide an estimation of the power spectrum over the frequency support where $\hat{\psi}_{j,k}$ is concentrated. For processes with power spectrums that decrease faster than a power law, we as well include in $\Lambda_{2,j}$ shifted two points interactions, of the form $\sum_n \varphi * \tilde{\psi}_{j,k}(2^{j-1}n) \varphi * \tilde{\psi}_{j,k}^*(2^{j-1}(n + \tau))$, with small τ .

The interaction terms (74) capture the interaction between wavelet coefficients at the scale $2^{j'}$ and scattering coefficients at a same scale $2^\ell = 2^{j'}$

$$\Lambda_{3,j}(\varphi_{j-1}) = \left(\sum_n |\varphi * \psi_{j,m}|^q * \psi_{j',k}(2^{j-1}n) \varphi * \psi_{j',k}^*(2^{j-1}n) \right)_{k,m \leq Q, j' \geq j}. \quad (78)$$

It is antisymmetric in φ and it captures phase alignment properties across scales. If $q = 2$ then they are third order polynomial moments in φ . When $q = 1$ these these coefficients capture similar properties [CMA⁺23]. The last interaction terms (75) give the interactions between wavelet modulus coefficients at different wavelet scales 2^j and $2^{j'}$ but at the same scattering scales 2^ℓ

$$\Lambda_{4,j}(\varphi_{j-1}) = \left(\sum_n |\varphi * \tilde{\psi}_{j,k'}|^q * \tilde{\psi}_{\ell,k}(2^{j-1}n) |\varphi * \tilde{\psi}_{j',k''}|^q * \tilde{\psi}_{\ell,k}^*(2^{j-1}n) \right)_{k,k',k'' \leq Q, \ell \geq j' \geq j}. \quad (79)$$

If $q = 2$ then they define fourth order moments. When $q = 1$ they have similar numerical properties [CMA⁺23]. The largest number of coefficients is within $\Lambda_{4,j}$. The dimension of Ψ_j is of the order of $Q^3(j - J)^2$.

Further dimensionality reduction If φ has a probability distribution which is invariant to rotations, then the energy remains invariant to the flipping operator which transforms $\varphi(n)$ into $\varphi(-n)$. Since $\tilde{\psi}_{j,k}(-n) = \tilde{\psi}_{j,k}^*(n)$, one can verify, similarly to [MZR20, MRL⁺23], that the imaginary parts of $\Lambda_{3,j}$ and $\Lambda_{4,j}$ change sign when $\varphi(n)$ is transformed into $\varphi(-n)$. It results that the interaction coefficients of the energy U_θ over these imaginary parts are zero. We impose this property in all numerical examples shown in this paper by eliminating the imaginary parts of $\Lambda_{3,j}$ and $\Lambda_{4,j}$ from Ψ_j . We also point out that for a symmetrical process, such that φ and $-\varphi$ have the same distribution, one can as well discard $\Lambda_{3,j}$.

C Estimation of Conditional Energy parameters

C.1 Interaction energy estimation by score matching

Instead of minimizing directly each term $\mathbb{E}_{p_j}(KL(\bar{p}_j, \bar{p}_{\bar{\theta}_j}))$, and applying the algorithm in (10), which requires heavy calculations, we use a score matching algorithm which minimizes a relative Fisher information. It is calculated with a gradient relatively to $\bar{\varphi}_j$, which eliminates the free energy $F_j(\varphi_j)$. The corresponding Fisher information is averaged with p_j :

$$\mathbb{E}_{p_j}(\mathcal{I}(\bar{p}_{\bar{\theta}_j}, \bar{p}_j)) = \mathbb{E}_{p_j} \mathbb{E}_{\bar{p}_j} \left(\|\nabla_{\bar{\varphi}_j} \log \bar{p}_j(\bar{\varphi}_j | \varphi_j) - \nabla_{\bar{\varphi}_j} \log \bar{p}_{\bar{\theta}_j}(\bar{\varphi}_j | \varphi_j)\|^2 \right).$$

According to [HD05] and similarly to (11), since $\nabla_{\bar{\varphi}_j} \log \bar{p}_{\bar{\theta}_j} = \bar{\theta}_j^T \nabla \Psi_j$, one can verify that it is equivalent to minimize

$$\ell(\bar{\theta}_j) = \mathbb{E}_{p_{j-1}} \left(\frac{1}{2} \|\bar{\theta}_j^T \nabla_{\bar{\varphi}_j} \Psi_j(\varphi_{j-1})\|^2 - \bar{\theta}_j^T \Delta_{\bar{\varphi}_j} \Psi_j(\varphi_{j-1}) \right). \quad (80)$$

This calculation can be done in parallel for all j .

Like eq. (12), a closed form for the minimizing $\bar{\theta}_j$ is given by

$$\bar{\theta}_j = \bar{M}_j^{-1} \mathbb{E}_{p_{j-1}}(\Delta_{\bar{\varphi}_j} \Psi_j(\varphi_{j-1})) \quad \text{with} \quad \bar{M}_j = \mathbb{E}_{p_{j-1}}(\nabla_{\bar{\varphi}_j} \Psi_j(\varphi_{j-1}) \nabla_{\bar{\varphi}_j} \Psi_j(\varphi_{j-1})^T) \quad (81)$$

For considered datasets, with the potential Ψ_j from eq. (55), (80) is an ill-conditioned quadratic learning problem. We compute the matrix \bar{M}_j from eq. (81), and precondition θ , by defining $\tilde{\theta}_j = (\bar{M}_j + \epsilon \text{Id})^{1/2} \bar{\theta}_j$, whose optimal value can be computed by minimizing the quadratic loss

$$\tilde{\ell}(\tilde{\theta}) = \frac{1}{2} \tilde{\theta}_j^T \tilde{\theta}_j - \tilde{\theta}_j^T \mathbb{E}_{p_{j-1}}((\bar{M}_j + \epsilon \text{Id})^{-1/2} \Delta_{\bar{\varphi}_j} \Psi_j(\varphi_{j-1})),$$

which has a condition number of 1. This loss function is minimized using a single batch gradient descent. The same procedure applies to θ_j , at the coarsest scale, for the quadratic loss defined in eqs. (11) and (12). Due to the finite size of the datasets, the expectancies are replaced with their empirical estimations. For applications in this paper, we used, for ϵ , values not bigger than 10% of the eigenvalues of \bar{M}_j .

C.2 Free energy calculation

To derive the Gibbs energy $U_\theta(\varphi)$ in equation (30), we define and optimize a linear approximation $F_{\alpha_j} = \alpha_j^T \Phi_j$ of the free energy F_j defined by the normalization integral (29) of $\bar{p}_{\bar{\theta}_{j-1}}$. Taking the derivative with respect to φ_j in (29) gives

$$\nabla_{\varphi_j} F_j(\varphi_j) - \mathbb{E}_{\bar{p}_{\bar{\theta}_j}(\bar{\varphi}_j|\varphi_j)}(\bar{\theta}_j^T \nabla_{\varphi_j} \Psi_j(\varphi_{j-1})) = 0. \quad (82)$$

Using the previous equation, it can be proven that the free energy F_j is a minimizer of the quadratic function $f \mapsto \mathbb{E}_{\bar{p}_{\bar{\theta}_j}(\bar{\varphi}_j|\varphi_j)p_j(\varphi_j)}(\|\nabla_{\varphi_j} f(\varphi_j) - \bar{\theta}_j^T \nabla_{\varphi_j} \Psi_j(\varphi_{j-1})\|^2)$. The parameters α_j are optimized with the quadratic loss

$$\ell(\alpha_j) = \mathbb{E}_{\bar{p}_{\bar{\theta}_j}(\bar{\varphi}_j|\varphi_j)p_j(\varphi_j)}(\|\alpha_j^T \nabla_{\varphi_j} \Phi_j(\varphi_j) - \bar{\theta}_j^T \nabla_{\varphi_j} \Psi_j(\varphi_{j-1})\|^2). \quad (83)$$

This expected value is calculated with an empirical average over the m samples $\varphi_j^{(i)}$ of p_j . For each $\varphi_j^{(i)}$ we know a sample $\bar{\varphi}_j^{(i)}$ of $\bar{p}_j(\bar{\varphi}_j|\varphi_j^{(i)})$. We modify this sample with a MALA algorithm to obtain a sample of $\bar{p}_{\bar{\theta}_j}(\bar{\varphi}_j|\varphi_j^{(i)})$, which approximates $\bar{p}_j(\bar{\varphi}_j|\varphi_j^{(i)})$.

D Moment errors on φ^4

Metric on moments We evaluate the model errors from generated sampled over a sufficient set of moments. For φ^4 , these statistics are second order moments and the marginal distribution of $\varphi(n)$. This appendix defines a Kullback-divergence error from these moments.

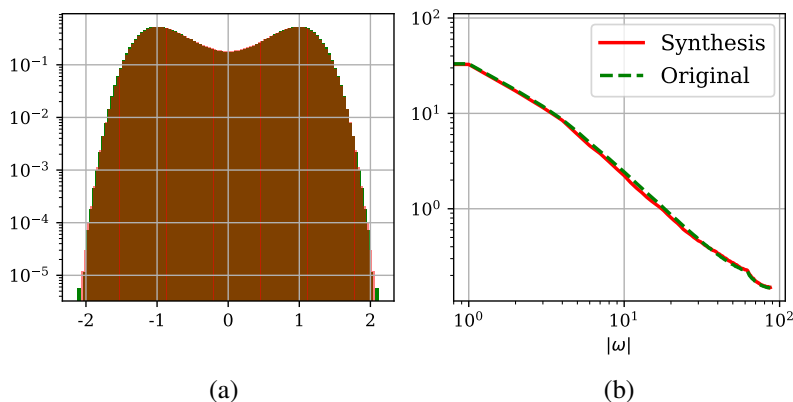


Figure 15: (a): The marginal probability distribution of each $\varphi(n)$ is computed from samples of the φ^4 model at the phase transition. It is superimposed with the marginal probability distribution of samples of the hierarchic model in a Haar wavelet basis. (b): Eigenvalues of covariance matrices in the Fourier basis. They are computed from samples of the φ^4 model and with the Haar hierarchic model, for images of size $d = 128^2$. The hierarchic model recovers precisely both types of moments in (a) and (b), which are sufficient statistics for φ^4 .

The φ^4 model has a Gibbs energy $U(\varphi) = \theta^T \Phi(\varphi)$, where Φ is defined in (51), with a single scalar potential $\Gamma(\varphi * \phi_\ell) = \Gamma(\varphi)$ for $\ell = 0$. Sections 2.2 shows that p is equal to the maximum entropy distribution p_θ such that $\mathbb{E}_{p_\theta}(\Phi) = \mathbb{E}_p(\Phi)$. These moments specified by the covariance C of $p(\varphi)$ and by the marginal distribution $\tilde{p}(t)$ of field values $t = \varphi(n)$.

To evaluate the precision of a hierarchic model p_θ , we evaluate the covariance C_θ and the marginal distribution $\tilde{p}_\theta(t)$, with a Monte Carlo average over samples generated by this model. We compute the KL divergence between the maximum entropy distributions having covariances a C and a C_θ . Both distributions are gaussians and their KL divergence is

$$\frac{1}{2} \log(|C_\theta C^{-1}|) - \frac{d}{2} + \frac{1}{2} \text{Tr } C C_\theta^{-1}.$$

The maximum entropy distributions having marginals \tilde{p} and \tilde{p}_θ are random vectors with d independent coordinates. Their KL divergence is thus $d KL(\tilde{p}, \tilde{p}_\theta)$. Adding and renormalizing these KL divergences by the dimension d gives an error:

$$\epsilon(p, p_\theta) = \frac{1}{2d} \log(|C_\theta C^{-1}|) - \frac{1}{2} + \frac{1}{2d} \text{Tr} C C_\theta^{-1} + KL(\tilde{p}, \tilde{p}_\theta). \quad (84)$$

Figure 15 shows that the estimated marginal distributions \tilde{p} and the eigenvalues of the covariance C of p are precisely approximated by the marginal \tilde{p}_θ and the covariance C_θ of the hierarchical model p_θ computed in a Haar basis.

E Proofs of Propositions and Theorems

E.1 Proof of Proposition 2.1

The log-Sobolev equation (2) implies a Poincaré inequality [Led00]

$$\mathbb{E}[|f(\varphi) - \mathbb{E}(f(\varphi))|^2] \leq 2c(p) \int \|\nabla f(\varphi)\|^2 p(\varphi) d\varphi.$$

This is proven, for regular enough functions f , by applying the log-Sobolev inequality to the density $q = p + \epsilon(pf - \mathbb{E}_p(f))$, and letting ϵ go to zero. Let e_{\max} be a normalized eigenvector of the covariance of p corresponding to the maximum eigenvalue μ_{\max} and $f(\varphi) = \langle e_{\max}, \varphi \rangle$. The Poincaré inequality applied to f gives

$$\mu_{\max} \leq 2c(p) \int \|e_{\max}\|^2 p(\varphi) d\varphi = 2c(p),$$

which proves that $c(p) \geq \mu_{\max}/2$.

E.2 Proof of Proposition 3.1

To prove that $KL(p, \tilde{q}) \leq KL(p, q)$, we decompose

$$KL(p, \tilde{q}) = \int p(\varphi) \log p(\varphi) d\varphi - \int p(\varphi) \log \tilde{q}(\varphi) d\varphi,$$

with $\tilde{q} = \tilde{\mathcal{Z}}^{-1} e^{-A \text{ve}_{j-1} U}$. Let us verify that the second term increases when \tilde{q} is replaced by $q = \mathcal{Z}^{-1} e^{-U}$.

Since p is translation invariant, a change of variable proves that

$$\begin{aligned} - \int p(\varphi) \log \tilde{q}(\varphi) d\varphi &= |\mathcal{G}_{j-1}|^{-1} \int p(\varphi) \sum_{\tau \in \mathcal{G}_{j-1}} U(T_\tau \varphi) d\varphi + \log \tilde{\mathcal{Z}} \\ &= \int p(\varphi) U(\varphi) d\varphi + \log \tilde{\mathcal{Z}}, \end{aligned} \quad (85)$$

where

$$\tilde{\mathcal{Z}} = \int e^{-A \text{ve}_{j-1} U(\varphi)} d\varphi = \int \prod_{\tau \in \mathcal{G}_{j-1}} (e^{-U(T_\tau \varphi)})^{|\mathcal{G}_{j-1}|^{-1}} d\varphi.$$

We now prove that

$$\tilde{\mathcal{Z}} \leq \mathcal{Z} = \int e^{-U(\varphi)} d\varphi, \quad (86)$$

so that we can show with (85) that

$$- \int p(\varphi) \log \tilde{q}(\varphi) d\varphi \leq - \int p(\varphi) q(\varphi) d\varphi,$$

which proves the theorem result (38).

We prove (86) by iterating on the Hölder inequality which proves that

$$\left(\int \prod_{\tau \in \mathcal{G}_{j-1}} (e^{-U(T_\tau \varphi)})^{|\mathcal{G}_{j-1}|^{-1}} d\varphi \right)^{|\mathcal{G}_{j-1}|} \leq \left(\int \prod_{\tau \in \mathcal{G}_{j-1} - \{\tau_1\}} (e^{-U(T_\tau \varphi)})^{(|\mathcal{G}_{j-1}|-1)^{-1}} d\varphi \right)^{|\mathcal{G}_{j-1}|-1} \int e^{-U(T_{\tau_1} \varphi)} d\varphi.$$

But $\int e^{-U(T_\tau \varphi)} d\varphi = \mathcal{Z}$ so reapplying $|\mathcal{G}_{j-1}| - 1$ times the Hölder inequality to the integral to the power $|\mathcal{G}_{j-1}| - 1$ proves that $(\tilde{\mathcal{Z}})^{|\mathcal{G}_{j-1}|} \leq (\mathcal{Z})^{|\mathcal{G}_{j-1}|}$ and hence $\tilde{\mathcal{Z}} \leq \mathcal{Z}$, which finishes the proof. \square

E.3 Proof of Theorem 4.1

At the coarsest scale 2^J , Φ_J is defined in (47) by a convolutional operator whose kernel is written K_J and a scalar potential defined in (48). One can thus verify that

$$\theta_J = (K_J/2, \gamma_J) \text{ and } \Phi_J(\varphi_J) = (\varphi_J * \varphi_J^T, \Gamma(\varphi_J)). \quad (87)$$

The potential Φ_J thus satisfies (51) for $j = J$.

To prove that the Φ_j define a hierarchic potential, we shall prove that for any $j \geq J$, if

$$\Phi_j(\varphi_j) = (\varphi_j * \varphi_j^T, \Gamma(\varphi_j * \phi_\ell))_{J-j \geq \ell \geq 0}$$

and if Ψ_j is defined by (49) and hence

$$\Psi_j(\varphi_{j-1}) = (\bar{\varphi}_j \bar{\varphi}_j^T, \bar{\varphi}_j \varphi_j^T, \Gamma(\varphi_{j-1}))$$

then $\text{Ave}_{j-1}(\Phi_j, \Psi_j)$ is a linear function of Φ_{j-1} , with

$$\Phi_{j-1}(\varphi_{j-1}) = (\varphi_{j-1} * \varphi_{j-1}^T, \Gamma(\varphi_{j-1} * \phi_\ell))_{J-j+1 \geq \ell \geq 0}.$$

Let us first show that $\text{Ave}_{j-1}(\Psi_j)$ is a linear function of Φ_{j-1} . We consider the first two terms of Ψ_j . Since $\bar{\varphi}_j = \bar{G}\varphi_{j-1}$ and $\varphi_j = G\varphi_{j-1}$, it results that $\bar{\varphi}_j \bar{\varphi}_j^T$ and $\bar{\varphi}_j \varphi_j^T$ are linear functions of $\varphi_{j-1} \varphi_{j-1}^T$. Since $\varphi_{j-1} \varphi_{j-1}^T = (\varphi_{j-1}(n) \varphi_{j-1}(n'))_{n, n'}$ it results that

$$\begin{aligned} \text{Ave}_{j-1}(\varphi_{j-1} \varphi_{j-1}^T) &= |\mathcal{G}_{j-1}|^{-1} \left(\sum_{\tau \in \mathcal{G}_{j-1}} \varphi_{j-1}(n - \tau) \varphi_{j-1}(n' - \tau) \right)_{n, n'} \\ &= |\mathcal{G}_{j-1}|^{-1} (\varphi_{j-1} * \varphi_{j-1}^T(n' - n))_{n, n'}. \end{aligned}$$

It results that applying Ave_{j-1} to the first two terms of Ψ_{j-1} is a linear function of Φ_{j-1} . For the third term of $\text{Ave}_{j-1}(\Psi_j)$ we have

$$\text{Ave}_{j-1} \Gamma(\varphi_{j-1}) = \Gamma(\varphi_{j-1}) = \Gamma(\varphi_{j-1} * \phi_0),$$

because $\phi_0 = \delta$, which is a linear function of the second term of Ψ_j which includes this term. It concludes the proof that $\text{Ave}_{j-1}(\Psi_j)$ is a linear function of Φ_{j-1} .

Let us now prove that $\text{Ave}_{j-1}(\Phi_j)$ is a linear function of Φ_{j-1} . For the first term in $\text{Ave}_{j-1}(\Phi_j)$, equation (64), which states that $\varphi_j(n) = \varphi_{j-1} * g(2n)$, gives

$$\begin{aligned} \varphi_j * \varphi_j^T &= \left(\sum_{\tau \in \mathcal{G}_j} \varphi_j(-\tau) \varphi_j(n - \tau) \right)_n \\ &= \left(\sum_{\tau \in \mathcal{G}_j} (\varphi_{j-1} * g)(-2\tau) (\varphi_{j-1} * g)(2n - 2\tau) \right)_n. \end{aligned}$$

Averaging over all the translations on the grid \mathcal{G}_{j-1} eliminates the subsampling in the previous sum, and gives

$$\begin{aligned} \text{Ave}_{j-1}(\varphi_j * \varphi_j^T) &= \frac{1}{4} ((\varphi_{j-1} * g) * (\varphi_{j-1}^T * g^T)(2n))_n \\ &= \frac{1}{4} ((g * g^T) * (\varphi_{j-1} * \varphi_{j-1}^T)(2n))_n, \end{aligned}$$

where $g^T(n) = g(-n)$. $\text{Ave}_{j-1}(\varphi_j * \varphi_j^T)$ is thus a linear transformation of the first term of $\Phi_{j-1}(\varphi_{j-1})$.

To compute the second terms of $\text{Ave}_{j-1}(\Phi_j)$, we use (67) which shows that

$$\varphi_j * \phi_\ell(n) = \varphi_{j-1} * \phi_{\ell+1}(2n). \quad (88)$$

Moreover Γ computes a sum on the grid \mathcal{G}_j of pointwise transformations ρ_k which commute with translations. It results that the averaging of all translations on the grid \mathcal{G}_{j-1} gives

$$\begin{aligned} \text{Ave}_{j-1}(\Gamma(\varphi_j * \phi_\ell)) &= |\mathcal{G}_{j-1}|^{-1} \left(\sum_{\tau \in \mathcal{G}_{j-1}, n \in \mathcal{G}_j} \rho_k(\varphi_{j-1} * \phi_{\ell+1}(2n - \tau)) \right)_k \\ &= \frac{1}{4} \left(\sum_{n \in \mathcal{G}_{j-1}} \rho_k(\varphi_{j-1} * \phi_{\ell+1}(n)) \right)_k \\ &= \frac{1}{4} \Gamma(\varphi_{j-1} * \phi_{\ell+1}). \end{aligned}$$

This proves that the second terms of $\text{Ave}_{j-1}(\Phi_j)$ is a linear function of the second term of Φ_{j-1} . This finishes the proof that the Φ_j define a stationary hierarchic potential.

Observe that the scalar potential of each interaction energy Ψ_j creates a scalar potential at each scale, which appears in (51). If we approximate the free energies F_j by $\alpha_j^T \Phi_j$ then Proposition 3.2 defines stationary energy models $U_{\theta_j} = \theta_j^T \Phi_j$ at each scale 2^j . The coupling vector θ_{j-1} is calculated from θ_j and $(\bar{\theta}_j, \alpha_j)$ with the operator Q_j . It defines a fine scale stationary energy model

$$U_{\theta}(\varphi) = \theta_0^T \Phi_0(\varphi) = (K, \gamma_j)_{j \geq J}^T (\varphi * \varphi^T, \Gamma(\varphi * \phi_j))_{J \geq j \geq 0},$$

and hence

$$U_{\theta}(\varphi) = \frac{1}{2} \varphi^T K \varphi + \sum_{j=0}^J \gamma_j^T \Gamma(\varphi * \varphi_j),$$

which finishes the theorem proof.

E.4 Proof of Theorem 5.1

To verify that the Φ_j define a hierarchic potential we shall prove that for any $j \geq J$, if

$$\Phi_j(\varphi_j) = (R(\varphi_j) * R(\varphi_j)^T, \Gamma(\varphi_j * \phi_{\ell}))_{J-j \geq \ell \geq 0} \quad \text{with } R(\varphi_j) = (\varphi_j, |\varphi * \tilde{\psi}_{j',k'}(2^j n)|^q)_{j' > j, k'},$$

and

$$\Psi_j = (S_j S_{j'}^T, \Gamma)_{J+1 \geq j' \geq j} \quad \text{with } S_{j'}(\varphi_{j-1}) = \left(\varphi * \tilde{\psi}_{j',k'}(2^{j-1} n), |\varphi * \tilde{\psi}_{j',k'}|^q * \psi_{\ell,k}(2^{j-1} n) \right)_{\ell \geq j', k, k' \leq Q, n},$$

then $\text{Ave}_{j-1}(\Phi_j)$ and $\text{Ave}_{j-1}(\Psi_j)$ are linear functions of Φ_{j-1} , for

$$\Phi_{j-1}(\varphi_{j-1}) = (R(\varphi_{j-1}) * R(\varphi_{j-1})^T, \Gamma(\varphi_{j-1} * \phi_{\ell}))_{J-j+1 \geq \ell \geq 0}.$$

From the proof of Theorem 4.1, the Γ -terms of $\text{Ave}_{j-1}(\Phi_j)$ and $\text{Ave}_{j-1}(\Psi_j)$ are linear functions of the Γ -terms of Φ_{j-1} . We concentrate the first terms in $\text{Ave}_{j-1}(\Psi_j)$ and $\text{Ave}_{j-1}(\Phi_j)$.

For $\text{Ave}_{j-1}(\Psi_j)$, consider $\text{Ave}_{j-1}(S_j S_{j'}^T)$. For any $j' \geq j$, the scattering vector $S_{j'}$ is a linear function of $R(\varphi_{j-1}) = (\varphi_{j-1}, |\varphi * \tilde{\psi}_{j',k'}(2^{j-1} n)|^q)_{j' > 0, k' \leq Q}$. Nonlinear terms in $S_{j'}$ are included in $R(\varphi_{j-1})$, and, from (71), $\varphi * \tilde{\psi}_{j',k'}(2^{j-1} n)$, is a linear function of φ_{j-1} .

It results that the terms $\text{Ave}_{j-1}(S_j S_{j'}^T)$ are linear functions of $\text{Ave}_{j-1}(R_{j-1} R_{j-1}^T)$. In the same way that we proved for Theorem 4.1 that $\text{Ave}_{j-1}(\varphi_{j-1} \varphi_{j-1}^T)$ is a linear function of $\varphi_{j-1} * \varphi_{j-1}^T$, we prove that $\text{Ave}_{j-1}(R(\varphi_{j-1}) R(\varphi_{j-1})^T)$ is a linear function of $R(\varphi_{j-1}) * R(\varphi_{j-1})^T$. The term $\text{Ave}_{j-1}(S_j S_{j'}^T)$ is therefore a linear function of the first term of Φ_{j-1} .

Let us now prove that the first term of $\text{Ave}_{j-1}(\Phi_j)$, and hence $\text{Ave}_{j-1}(R(\varphi_j) * R(\varphi_j)^T)$, is a linear function of $R(\varphi_{j-1}) * R(\varphi_{j-1})^T$.

$R(\varphi_j)$ is deduced from $R(\varphi_{j-1})$ using, the filter G on φ_{j-1} , and by subsampling (or discarding) the nonlinear terms.

$\text{Ave}_{j-1}(R(\varphi_j) R(\varphi_j)^T)$, is a linear function of $\text{Ave}_{j-1}(R(\varphi_{j-1}) R(\varphi_{j-1})^T)$, which is itself a linear transform of $R(\varphi_{j-1}) * R(\varphi_{j-1})^T$.

This finishes the proof that the Φ_j define a stationary hierarchic potential.

Proposition 3.2 implies that approximating F_j by $\alpha_j^T \Phi_j$ yields a coupling flow equation (41). It computes θ_{j-1} from θ_j and $(\bar{\theta}_j, \alpha_j)$ with the linear operator Q_j . It defines

$$U_{\theta}(\varphi) = \theta_0^T \Phi_0(\varphi) = \theta_0^T (R(\varphi) * R(\varphi)^T, \Gamma(\varphi * \phi_{\ell}))_{J \geq j \geq 0}.$$

Since $R(\varphi) = (\varphi, |W\varphi|^q)$, for $\theta_0 = (K, L, M, \gamma_j)_{j \geq J}$ where (K, L, M) are convolutional operators, this can be rewritten

$$U_{\theta}(\varphi) = \frac{1}{2} \varphi^T K \varphi + \varphi^T L (|W\varphi|^q) + \frac{1}{2} (|W\varphi|^q)^T M (|W\varphi|^q) + \sum_{j=0}^J \gamma_j^T \Gamma(\varphi * \phi_j),$$

which proves (59).

F Estimation Algorithms

F.1 Normalized Autocorrelation Relaxation Time of a Langevin Diffusion

This appendix specifies the calculation of normalized relaxation time of Langevin diffusions in hierarchic models.

Conditional auto-correlation relaxation time As in [MOBM22, GLBM23], we compute the auto-correlation relaxation time (8) to sample the conditional probabilities of a hierarchic model with an unadjusted Langevin diffusion. This conditional probability has an energy $\bar{U}_{\bar{\theta}_j}$. The unadjusted Langevin diffusion of $\bar{\varphi}_j$ is numerically computed with an Euler-Maruyama discretization with a time interval δ_j . This time interval must be smaller than the inverse of the Lipschitz constant of $\nabla_{\bar{\varphi}_j} \bar{U}_{\bar{\theta}_j}$ [VW22]. This Lipschitz constant is evaluated by estimating the supremum of the eigenvalues of the Hessian $\nabla_{\bar{\varphi}_j}^2 \bar{U}_{\bar{\theta}_j}(\varphi_{j-1})$ over typical realizations φ_{j-1} . We set δ_j to be a fixed fraction of the inverse of this supremum.

Let $\bar{\varphi}_{j,\alpha}$ be the wavelet coefficients of obtained by the Langevin diffusion, after α steps at intervals δ_j , thus corresponding to a time $t = \alpha \delta_j$. A normalized conditional auto-correlation at α is

$$\bar{A}_j(\alpha|\varphi_j) = \frac{\mathbb{E}_{\bar{p}_{\bar{\theta}_j}(\cdot|\varphi_j)}((\bar{\varphi}_{j,\alpha} - \mathbb{E}_{\bar{p}_{\bar{\theta}_j}(\cdot|\varphi_j)}(\bar{\varphi}_j))(\bar{\varphi}_{j,0} - \mathbb{E}_{\bar{p}_{\bar{\theta}_j}(\cdot|\varphi_j)}(\bar{\varphi}_j)))}{\mathbb{E}_{\bar{p}_{\bar{\theta}_j}(\cdot|\varphi_j)}((\bar{\varphi}_j - \mathbb{E}_{\bar{p}_{\bar{\theta}_j}(\cdot|\varphi_j)}(\bar{\varphi}_j))^2)}, \quad (89)$$

This auto-correlation is averaged over the distribution of φ_j

$$A_j(\alpha) = \mathbb{E}_{p_j}(\bar{A}_j(\alpha|\varphi_j)). \quad (90)$$

The exponential decay $A_j(\alpha)$ is measured by the normalized autocorrelation relaxation time $\bar{\tau}_j$,

$$A_j(\alpha) \approx A_j(0) \exp\left(-\frac{\alpha}{\bar{\tau}_j}\right). \quad (91)$$

This normalized relaxation time is the number of Langevin iterations needed to reach a fixed precision.

Comments on MALA The rejection step of the MALA algorithm modifies the value of the relaxation time. Whereas Langevin and MCMC algorithm have hierarchical autocorrelation relaxation times which do not depend upon the system size d , the MALA algorithm produces a hierarchical relaxation time which has a slow growth as a function of d , highlighted in [GLBM23]. Indeed, MALA relies on a global acceptance step, which does not take advantage of the locality of interactions, as opposed to an MCMC sampling or an unadjusted Langevin diffusion [MOBM22, MS06]. For example, MALA has a mixing time that grows with the dimension d , for strongly log-concave distributions having a log-Sobolev constant which does not depend on d [CEL⁺21, LZT22, WSC22], whereas it is not the case for an MCMC sampling or a Langevin unadjusted diffusions. However, MALA is the fastest algorithm to compute the hierarchic sampling for the image sizes considered in this paper [GLBM23]. It is used for the generation results but not to evaluate the relaxation time in order to avoid issues related to the rejection-approval step.

F.2 Estimation of the Bi-spectrum

We describe the calculation of the bi-spectrum in Figure 12. The bi-spectrum is defined as the expected value Fourier transform of the 3 points correlation function. We use a regularized estimation of these statistics for rotationally invariant probability distributions, described in [CMA⁺23]. It performs a frequency averaging in thin frequency annuli, evenly spaced in frequency log-scale, that we write \mathcal{A}_k . For the Figure 12(e), for images of size $d = 128^2$, the frequency plane is decomposed into 9 frequency annuli \mathcal{A}_k , which select frequencies ω such that $2^{-7k/9}\pi \leq |\omega| \leq 2^{-7(k+1)/9}\pi$.

We consider probability distributions which are invariant to rotations. The power spectrum is thus estimated with an average over frequencies ω in each annulus \mathcal{A}_k and over multiple samples $\varphi^{(i)}$:

$$P(k) = \text{Ave}_{i,\omega \in \mathcal{A}_k} |\hat{\varphi}^{(i)}(\omega)|^2. \quad (92)$$

For (k_1, k_2, k_3) , a regularized normalized bi-spectrum is defined as a sum over all $(\omega_1, \omega_2, \omega_3)$ from 3 frequencies $\omega_j \in \mathcal{A}_{k_j}$ which sum to zero $\sum_{j=1}^3 \omega_j = 0$, by multiplying the Fourier transforms at these frequencies of multiple samples $\varphi^{(i)}$:

$$B(k_1, k_2, k_3) = \text{Ave}_{i,\omega_j \in \mathcal{A}_{k_j}, \sum_{j=1}^3 \omega_j = 0} \left(\frac{\hat{\varphi}(\omega_1^{(i)}) \hat{\varphi}(\omega_2^{(i)}) \hat{\varphi}(\omega_3^{(i)})}{\sqrt{P(k_1) P(k_2) P(k_3)}} \right). \quad (93)$$

References

- [ABBL06] Alexei Andreanov, Giulio Biroli, Jean-Philippe Bouchaud, and Alexandre Lefevre. Field theories and exact stochastic equations for interacting particle systems. *Physical Review E*, 74(3):030101, 2006.
- [ABT18] Richard C Aster, Brian Borchers, and Clifford H Thurber. *Parameter estimation and inverse problems*. Elsevier, 2018.
- [AGV13] Patrice Abry, Paolo Goncalves, and Jacques Lévy Véhel. *Scaling, fractals and wavelets*. John Wiley & Sons, 2013.
- [Bat99] Guy Battle. *Wavelets and renormalization*, volume 10. World Scientific, 1999.
- [BB19] Roland Bauerschmidt and Thierry Bodineau. A very simple proof of the lsi for high temperature spin systems. *Journal of Functional Analysis*, 276(8):2582–2588, 2019.
- [BBD23] Roland Bauerschmidt, Thierry Bodineau, and Benoit Dagallier. Stochastic dynamics and the polchinski equation: an introduction. *arXiv preprint arXiv:2307.07619*, 2023.
- [BD22] Roland Bauerschmidt and Benoit Dagallier. Log-sobolev inequality for near critical ising models. *arXiv preprint arXiv:2202.02301*, 2022.
- [BDSG⁺15] Lorenzo Bertini, Alberto De Sole, Davide Gabrielli, Giovanni Jona-Lasinio, and Claudio Landim. Macroscopic fluctuation theory. *Reviews of Modern Physics*, 87(2):593, 2015.
- [BGL⁺14] Dominique Bakry, Ivan Gentil, Michel Ledoux, et al. *Analysis and geometry of Markov diffusion operators*, volume 103. Springer, 2014.
- [Bis06] Christopher Bishop. Pattern recognition and machine learning. *Springer google schola*, 2:5–43, 2006.
- [BJPV98] Tomas Bohr, Mogens H. Jensen, Giovanni Paladin, and Angelo Vulpiani. *Dynamical Systems Approach to Turbulence*. Cambridge Nonlinear Science Series. Cambridge University Press, 1998.
- [CCL⁺20] Lok Hang Chan, Kun Chen, Chunxue Li, Chung Wang Wong, and Chun Yip Yau. On higher-order moment and cumulant estimation. *Journal of Statistical Computation and Simulation*, 90(4):747–771, 2020.
- [CE22] Yuansi Chen and Ronen Eldan. Localization schemes: A framework for proving mixing bounds for markov chains. In *2022 IEEE 63rd Annual Symposium on Foundations of Computer Science (FOCS)*, pages 110–122. IEEE, 2022.
- [CEL⁺21] Sinho Chewi, Murat A. Erdogdu, Mufan Bill Li, Ruoqi Shen, and Matthew Zhang. Analysis of langevin monte carlo from poincaré to log-sobolev, 2021.
- [CMA⁺23] Sihao Cheng, Rudy Morel, Erwan Allys, Brice Ménard, and Stéphane Mallat. Scattering spectra models for physics, 2023.
- [CMW92] Ronald R Coifman, Yves Meyer, and Victor Wickerhauser. Wavelet analysis and signal processing. In *In Wavelets and their applications*. Citeseer, 1992.
- [CR23] Jordan Cotler and Semon Rezchikov. Renormalizing diffusion models. *arXiv preprint arXiv:2308.12355*, 2023.
- [Dau92] Ingrid Daubechies. *Ten Lectures on Wavelets*. Society for Industrial and Applied Mathematics, 1992.
- [Del12] Bertrand Delamotte. *An Introduction to the Nonperturbative Renormalization Group*, page 49–132. Springer Berlin Heidelberg, 2012.
- [DLS02] Bernard Derrida, JL Lebowitz, and ER Speer. Large deviation of the density profile in the steady state of the open symmetric simple exclusion process. *Journal of statistical physics*, 107(3-4):599–634, 2002.
- [GCDBM22] Florentin Guth, Simon Coste, Valentin De Bortoli, and Stéphane Mallat. Wavelet score-based generative modeling. *Advances in Neural Information Processing Systems*, 2022.
- [GG84] Stuart Geman and Donald Geman. Stochastic relaxation, gibbs distributions, and the bayesian restoration of images. *IEEE Transactions on pattern analysis and machine intelligence*, (6):721–741, 1984.
- [GGR97] Andrew Gelman, Walter R Gilks, and Gareth O Roberts. Weak convergence and optimal scaling of random walk metropolis algorithms. *The annals of applied probability*, 7(1):110–120, 1997.
- [GLBM23] Florentin Guth, Etienne Lempereur, Joan Bruna, and Stéphane Mallat. Conditionally strongly log-concave generative models. *International Conference on Machine Learning*, 2023.
- [GM94] Ulf Grenander and Michael I Miller. Representations of knowledge in complex systems. *Journal of the Royal Statistical Society: Series B (Methodological)*, 56(4):549–581, 1994.
- [GNC10] Matan Gavish, Boaz Nadler, and Ronald R Coifman. Multiscale wavelets on trees, graphs and high dimensional data: theory and applications to semi supervised learning. In *ICML*, volume 10, pages 367–74, 2010.
- [Gro75] Leonard Gross. Logarithmic sobolev inequalities. *American Journal of Mathematics*, 97(4):1061–1083, 1975.
- [GRVE22] Marylou Gabrié, Grant M Rotskoff, and Eric Vanden-Eijnden. Adaptive monte carlo augmented with normalizing flows. *Proceedings of the National Academy of Sciences*, 119(10):e2109420119, 2022.
- [HD05] Aapo Hyvärinen and Peter Dayan. Estimation of non-normalized statistical models by score matching. *Journal of Machine Learning Research*, 6(4), 2005.

- [HK22] Truong Son Hy and Risi Kondor. Multiresolution matrix factorization and wavelet networks on graphs. In *ICML 2022 2nd AI for Science Workshop*, 2022.
- [HVG11] David K Hammond, Pierre Vandergheynst, and Rémi Gribonval. Wavelets on graphs via spectral graph theory. *Applied and Computational Harmonic Analysis*, 30(2):129–150, 2011.
- [Jaf92] Stephane Jaffard. Wavelet methods for fast resolution of elliptic problems. *SIAM Journal on Numerical Analysis*, 29(4):965–986, 1992.
- [Jaf04] Stephane Jaffard. Wavelet techniques in multifractal analysis. In *Proceedings of symposia in pure mathematics*, volume 72, pages 91–152, 2004.
- [Jay57] Edwin T Jaynes. Information theory and statistical mechanics. *Physical review*, 106(4):620, 1957.
- [Kad66] Leo P Kadanoff. Scaling laws for ising models near t c. *Physics Physique Fizika*, 2(6):263, 1966.
- [KHR22] Frederic Koehler, Alexander Heckett, and Andrej Risteski. Statistical efficiency of score matching: The view from isoperimetry. *arXiv preprint arXiv:2210.00726*, 2022.
- [KHY76] Leo P Kadanoff, Anthony Houghton, and Mehmet C Yalabik. Variational approximations for renormalization group transformations. *Journal of Statistical Physics*, 14(2):171–203, 1976.
- [KMR16] J. Kaupužs, R. V. N. Melnik, and J. Rimšāns. Corrections to finite-size scaling in the φ^4 model on square lattices. *International Journal of Modern Physics C*, 27(09):1650108, 2016.
- [kol41] A kolmogorov. Local structure of turbulence in an incompressible fluid at very high reynolds numbers. *CR Ad. Sei. USSR*, 30:305, 1941.
- [Kol42] AN Kolmogorov. Equations of turbulent motion of an incompressible fluid, izv. acad. sci., ussr. *Physics*, 6(1):2, 1942.
- [Kra67] Robert H Kraichnan. Inertial ranges in two-dimensional turbulence. *Physics of fluids*, 10(7):1417, 1967.
- [KS06] Jari Kaipio and Erkki Somersalo. *Statistical and computational inverse problems*, volume 160. Springer Science & Business Media, 2006.
- [Led00] Michel Ledoux. The geometry of markov diffusion generators. In *Annales de la Faculté des sciences de Toulouse: Mathématiques*, volume 9, pages 305–366, 2000.
- [LL13] Lev Davidovich Landau and Evgenii Mikhailovich Lifshitz. *Statistical Physics: Volume 5*, volume 5. Elsevier, 2013.
- [LS16] Tony Lelièvre and Gabriel Stoltz. Partial differential equations and stochastic methods in molecular dynamics. *Acta Numerica*, 25:681–880, 2016.
- [LZT22] Ruilin Li, Hongyuan Zha, and Molei Tao. Sqrt(d) dimension dependence of langevin monte carlo, 2022.
- [Mal89a] Stéphane Mallat. A theory for multiresolution signal decomposition: The wavelet representation. *IEEE Trans. Pattern Anal. Mach. Intell.*, 11:674–693, 1989.
- [Mal89b] Stéphane G Mallat. A theory for multiresolution signal decomposition: the wavelet representation. *IEEE transactions on pattern analysis and machine intelligence*, 11(7):674–693, 1989.
- [Mal09] Stéphane Mallat. *A wavelet tour of signal processing*. Academic Press, third edition edition, 2009.
- [Mal12] S. Mallat. Group invariant scattering. *Communications on Pure and Applied Mathematics*, 65(10):1331–1398, 2012.
- [Mey93] Yves Meyer. *Wavelets and Operators*, volume 1 of *Cambridge Studies in Advanced Mathematics*. Cambridge University Press, 1993.
- [MOBM22] Tanguy Marchand, Misaki Ozawa, Giulio Biroli, and Stéphane Mallat. Wavelet conditional renormalization group. *arXiv preprint arXiv:2207.04941*, 2022.
- [MRL⁺23] Rudy Morel, Gaspar Rochette, Roberto Leonarduzzi, Jean-Philippe Bouchaud, and Stéphane Mallat. Scale dependencies and self-similar models with wavelet scattering spectra. *Available at SSRN 4516767*, 2023.
- [MS06] Andrea Montanari and Guilhem Semerjian. Rigorous inequalities between length and time scales in glassy systems. *Journal of statistical physics*, 125:23–54, 2006.
- [MZR20] Stéphane Mallat, Sixin Zhang, and Gaspar Rochette. Phase harmonic correlations and convolutional neural networks. *Information and Inference: A Journal of the IMA*, 9(3):721–747, 2020.
- [Pod96] Rudolf Podgornik. Principles of condensed matter physics. p. m. chaikin and t. c. lubensky, cambridge university press, cambridge, england, 1995. *Journal of Statistical Physics*, 83:1263–1265, 06 1996.
- [Pol84] Joseph Polchinski. Renormalization and effective lagrangians. *Nuclear Physics B*, 231(2):269–295, 1984.
- [PS00] Javier Portilla and Eero P Simoncelli. A parametric texture model based on joint statistics of complex wavelet coefficients. *International journal of computer vision*, 40(1):49–70, 2000.
- [Ram20] Pierre Ramond. *Field theory: a modern primer*. Routledge, 2020.
- [RBL⁺22] Robin Rombach, Andreas Blattmann, Dominik Lorenz, Patrick Esser, and Björn Ommer. High-resolution image synthesis with latent diffusion models. In *Proceedings of the IEEE/CVF Conference on Computer Vision and Pattern Recognition*, pages 10684–10695, 2022.

- [RFB15] Olaf Ronneberger, Philipp Fischer, and Thomas Brox. U-net: Convolutional networks for biomedical image segmentation. In *Medical image computing and computer-assisted intervention—MICCAI 2015: 18th international conference, Munich, Germany, October 5–9, 2015, proceedings, part III 18*, pages 234–241. Springer, 2015.
- [RR98] Gareth O Roberts and Jeffrey S Rosenthal. Optimal scaling of discrete approximations to langevin diffusions. *Journal of the Royal Statistical Society: Series B (Statistical Methodology)*, 60(1):255–268, 1998.
- [Set21] James P Sethna. *Statistical Mechanics: Entropy, Order Parameters, and Complexity*, volume 14. Oxford University Press, USA, 2021.
- [Sim62] Herbert A Simon. The architecture of complexity. *Proceedings of the American philosophical society*, 106(6):467–482, 1962.
- [Sok91] Alan D. Sokal. How to beat critical slowing down: 1990 update. *Nucl. Phys. B Proc. Suppl.*, 20:55–67, 1991.
- [Sok97] Alan Sokal. Monte carlo methods in statistical mechanics: foundations and new algorithms. In *Functional integration: Basics and applications*, pages 131–192. Springer, 1997.
- [SSK⁺21] Yang Song, Jascha Sohl-Dickstein, Diederik P. Kingma, Abhishek Kumar, Stefano Ermon, and Ben Poole. Score-based generative modeling through stochastic differential equations. In *International Conference on Learning Representations*, 2021.
- [SZFA06] Kai Schneider, Jörg Züuber, Marie Farge, and Alexandre Azzalini. Coherent vortex extraction and simulation of 2d isotropic turbulence. *Journal of Turbulence*, (7):N44, 2006.
- [Täu14] Uwe C Täuber. *Critical dynamics: a field theory approach to equilibrium and non-equilibrium scaling behavior*. Cambridge University Press, 2014.
- [Tur18] Thomas Turk. *Matrix organisation*. Springer, 2018.
- [VNHM⁺20] Francisco Villaescusa-Navarro, ChangHoon Hahn, Elena Massara, Arka Banerjee, Ana Maria Delgado, Doogesh Kodi Ramanah, Tom Charnock, Elena Giusarma, Yin Li, Erwan Allys, Antoine Brochard, Cora Uhlemann, Chi-Ting Chiang, Siyu He, Alice Pisani, Andrej Obuljen, Yu Feng, Emanuele Castorina, Gabriella Contardo, Christina D. Kreisch, Andrina Nicola, Justin Alsing, Roman Scoccimarro, Licia Verde, Matteo Viel, Shirley Ho, Stephane Mallat, Benjamin Wandelt, and David N. Spergel. The quijote simulations. *The Astrophysical Journal Supplement Series*, 250(1):2, August 2020.
- [VW22] Santosh S. Vempala and Andre Wibisono. Rapid convergence of the unadjusted langevin algorithm: Isoperimetry suffices, 2022.
- [WF72] Kenneth G Wilson and Michael E Fisher. Critical exponents in 3.99 dimensions. *Physical Review Letters*, 28(4):240, 1972.
- [Wil71] Kenneth G Wilson. Renormalization group and critical phenomena. ii. phase-space cell analysis of critical behavior. *Physical Review B*, 4(9):3184, 1971.
- [WSC22] Keru Wu, Scott Schmidler, and Yuansi Chen. Minimax mixing time of the metropolis-adjusted langevin algorithm for log-concave sampling, 2022.
- [ZJ21] Jean Zinn-Justin. *Quantum Field Theory and Critical Phenomena: Fifth Edition*. Oxford University Press, 04 2021.
- [ZM21] Sixin Zhang and Stéphane Mallat. Maximum entropy models from phase harmonic covariances. *Applied and Computational Harmonic Analysis*, 53:199–230, 2021.